Check for updates

JGR Atmospheres

RESEARCH ARTICLE
10.1029/2022JD036799

Fast Atmospheric Response to a Cold Oceanic Mesoscale Patch in the North-Western Tropical Atlantic

C. Acquistapace[1], A. N. Meroni[2], G. Labbri[3], D. Lange[4], F. Späth[4], S. Abbas[4], and H. Bellenger[5]

[1]Institute for Geophysics and Meteorology, University of Cologne, Cologne, Germany, [2]Department of Earth and Environmental Sciences, University of Milano-Bicocca, Milan, Italy, [3]Department of Physics and Astronomy, University of Bologna, Bologna, Italy, [4]Institute of Physics and Meteorology, University of Hohenheim, Stuttgart, Germany, [5]LMD, CNRS, Paris, France

Abstract Low-level clouds over the tropical and sub-tropical oceans play a crucial role in the planetary radiative energy budget. However, they are challenging to model in climate simulations because they are affected by local processes that are still partially unknown. The control that mesoscale sea surface temperature (SST) structures have on the dynamics of the lower atmosphere on daily scales is emerging to be non-negligible and calls for more effort to be understood. During the EUREC^{4}A field campaign, two of the research vessels (R/Vs) involved in the experiment sampled the edge of a cold mesoscale SST patch in the north-western tropical Atlantic, crossing a gradient of roughly 0.75°C/100 km. The comprehensive set of instruments carried by the R/Vs allows an unprecedented characterization of the atmospheric response to the cold water forcing. The cold ocean patch weakens the vertical atmospheric mixing, reducing the boundary layer depth of roughly 200 m and the horizontal wind intensity of approximately 3 m s^{-1}. At the same time, the humidity content in the sub-cloud layer increases and these conditions decrease the latent heat flux (by roughly 80 W m^{-2}) and reduce vertical velocity fluctuations, making it less likely that moisture exceeds the lifting condensation level. As a consequence, fewer and thinner low-level clouds form over cold water. Independent satellite measurements are found to agree with the in situ observations. The observed link between sea temperature and low-level clouds highlights its importance in the puzzle of modeling the sea-air-cloud interactions.

Plain Language Summary Puffy clouds typically visible at sea strongly challenge climate models that struggle to represent their interaction with the sea surface and solar radiation. And as a consequence, these climate models cannot precisely estimate how much the Earth's temperature will increase 100 years from now and its uncertainty. We went into the western Atlantic ocean for a month in January–February 2020 to measure sea surface temperature and cloud properties and observe how these changes occur. We saw clouds grow deeper over the warm water patches, holding more water and eventually raining. Weaker winds and more humid air occur on cold patches. Satellite observations seem to record the same behavior over a larger area in the same region. We detected a clear difference in cloud properties and amounts over warm and cold patches from all sensors, recording essential evidence of a feature that is hard to predict. We hope these observations will help to properly simulate the intensity and signs of low-cloud feedback over warm and cold oceanic patches of water to improve climate models.

Key Points:

- Ship-based observations are used to characterize the lower atmospheric response to a cold patch in the north-western subtropical Atlantic
- Signatures in dynamical and thermodynamical atmospheric properties agree with a reduced vertical mixing over the cold patch
- Such a weaker vertical mixing is linked to a reduced shallow cloud cover because less moisture reaches the level of saturation

Supporting Information:

Supporting Information may be found in the online version of this article.

Correspondence to:

C. Acquistapace and A. N. Meroni,
cacquist@meteo.uni-koeln.de;
agostino.meroni@unimib.it

Citation:

Acquistapace, C., Meroni, A. N., Labbri, G., Lange, D., Späth, F., Abbas, S., & Bellenger, H. (2022). Fast atmospheric response to a cold oceanic mesoscale patch in the north-western tropical Atlantic. *Journal of Geophysical Research: Atmospheres*, *127*, e2022JD036799. https://doi.org/10.1029/2022JD036799

Received 18 MAR 2022
Accepted 12 OCT 2022

Author Contributions:

Conceptualization: C. Acquistapace, A. N. Meroni, G. Labbri, H. Bellenger
Data curation: C. Acquistapace, A. N. Meroni, G. Labbri, D. Lange, F. Späth, S. Abbas, H. Bellenger
Formal analysis: C. Acquistapace, A. N. Meroni
Investigation: C. Acquistapace, A. N. Meroni, G. Labbri, H. Bellenger
Methodology: C. Acquistapace, A. N. Meroni, S. Abbas, H. Bellenger

© 2022 The Authors.
This is an open access article under the terms of the Creative Commons Attribution-NonCommercial License, which permits use, distribution and reproduction in any medium, provided the original work is properly cited and is not used for commercial purposes.

1. Introduction

Low clouds over tropical oceans have a cooling impact on the Earth's radiation budget. They strongly reflect the incoming solar radiation (high albedo) and slightly reduce the terrestrial emission (Scott et al., 2020). They also impact the temperature and moisture of the marine boundary layer (Bretherton et al., 2013) and are crucial in modulating the air-sea interactions that influence the sea surface temperature (SST) patterns (Yuan et al., 2018). Stratocumulus clouds prevail where free tropospheric subsidence reinforces the atmospheric boundary layer (ABL) stability, while shallow cumuliform clouds develop where subsidence and ABL inversion are weaker, typically over warmer surfaces with a deeper ABL (Mieslinger et al., 2019).

Bony and Dufresne (2005) identify such clouds as the largest source of uncertainty in climate model predictions. Most climate models cannot realistically simulate low cloud processes and strongly diverge in the feedback to global warming (Zelinka et al., 2020). Recent observational studies show that in response to surface warming,

21698996, 2022, 21, Downloaded from https://agupubs.onlinelibrary.wiley.com/doi/10.1029/2022JD036799 by Cochrane France, Wiley Online Library on [02/12/2022]. See the Terms and Conditions (https://onlinelibrary.wiley.com/terms-and-conditions) on Wiley Online Library for rules of use; OA articles are governed by the applicable Creative Commons License

Project Administration: C. Acquistapace, A. N. Meroni
Resources: C. Acquistapace, A. N. Meroni, G. Labbri, D. Lange, F. Späth
Software: C. Acquistapace, A. N. Meroni
Supervision: C. Acquistapace, A. N. Meroni, H. Bellenger
Validation: C. Acquistapace, A. N. Meroni, G. Labbri, H. Bellenger
Visualization: C. Acquistapace, A. N. Meroni, G. Labbri, H. Bellenger
Writing – original draft: C. Acquistapace, A. N. Meroni
Writing – review & editing: C. Acquistapace, A. N. Meroni, G. Labbri, D. Lange, F. Späth, S. Abbas, H. Bellenger

the marine tropical low cloud cover decreases (McCoy et al., 2017). Theory, high-resolution modeling and observations show that decreasing tropical cloud amounts bring a positive shortwave effect (Cesana et al., 2019). However, tropical cloud amount ultimately depends on processes occurring at different scales, like large-scale subsidence, boundary layer moisture budget, radiative cooling, and vertical turbulent fluxes, that are difficult to parameterize in numerical models (Ceppi et al., 2017). Many models continue to underestimate the low-level cloud amount, and they cannot reproduce the loss in low-level clouds due to increased SST observed in present climate conditions (Cesana & Waliser, 2016). The discrepancies between the modeled responses depend on how the coupling among convective mixing, turbulent fluxes, and low-cloud radiative effects are represented (Bony et al., 2017).

To get more accurate climate predictions, we need to properly model the intensity and sign of low-cloud feedback in a warming climate scenario. Thus, we need to understand the main controlling factors governing shallow cumulus clouds' macro and microphysical properties. Mieslinger et al. (2019), using satellite data, show that the shallow cumulus cloud fraction increases with increasing surface wind speed, Bowen ratio, and lower tropospheric stability. At the same time, it decreases by increasing SST or total column water vapor. The SST daily values have also been shown to influence the spatial patterns of shallow convection cumuli (Bony et al., 2020). Not only do local environmental variables affect cloud cover, but also previous meteorological conditions, as shown by Mauger and Norris (2010) with backward Lagrangian trajectory techniques. On seasonal and synoptic time scales, a combination of meteorological parameters is found to control the trade low-level clouds variability. In particular, wind speed is important on monthly time scales, together with relative humidity (RH) and surface sensible heat flux on synoptic scales (Brueck et al., 2015).

Mesoscale spatial structures of SST (on scales of 10–1,000 km) are known to modify the lower atmosphere mainly by two complementary mechanisms. On the one hand, they change the stability of the air column and its associated vertical mixing, and, on the other hand, they induce pressure gradients that generate secondary circulations. In the Downward Momentum Mixing (DMM) mechanism (Hayes et al., 1989; Wallace et al., 1989), when the wind flows from cold to warm water, the enhanced vertical mixing of horizontal momentum on the warm side of the front accelerates the surface wind. Thus, surface divergence appears over SST fronts. Instead, following the Pressure Adjustment (PA) mechanism (Lindzen & Nigam, 1987), surface wind convergence is generated over the SST maxima, as the warm SST patches generate surface pressure lows.

In the literature, several examples show how both mechanisms can act over short time scales (from hourly to weekly), inducing an atmospheric response in terms of surface wind, low-level clouds, and rainfall (Small et al., 2008). Frenger et al. (2013) show that mesoscale eddies in the Southern Ocean control the atmospheric response (wind, clouds, and rainfall) through the DMM on weekly time scales. Similar behaviors are observed over mesoscale eddies of all Western Boundary Currents (e.g., Chen et al., 2017; Liu et al., 2018; J. Ma et al., 2015; Rouault et al., 2016). In the Mediterranean Sea, the DMM modulates, on daily time scales, the surface wind speed and divergence (Meroni et al., 2020), with effects on the horizontal wind within the ABL, the cloud cover, and the rainfall probability (Desbiolles et al., 2021). In the tropical oceans, there are examples of the action of the PA mechanism over daily and weekly scales. By looking at SST and rainfall satellite data, Li and Carbone (2012) show that the PA is responsible for the convective rainfall excitation in the western Pacific warm pool. Using remote sensing observational products, Z. Ma et al. (2020) find that the cold wake of tropical cyclones induces a secondary circulation with effects on clouds and rainfall through the PA mechanism (Pasquero et al., 2021). Then, such an atmospheric response has a non-negligible impact on the top-of-the-atmosphere (TOA) radiation budget (Zhang et al., 2021). In particular, both the TOA downward short-wave flux and the TOA upward long-wave flux increase over the cold wakes of tropical cyclones, with a net TOA warming (cooling) during the day (night) of about 2 W m^{-2}. The works by Gaube et al. (2019) and Shao et al. (2019) highlight the importance of high-resolution and in situ observations to characterize the complex and fast atmospheric response to sub-mesoscale SST structures (on scales of 0.1–10 km). Rare examples of in situ evidence of the cloud response to the SST forcing are the works in the Kuroshio Extension region by Wang et al. (2019) and Tomita et al. (2013). They show, respectively, that a warm eddy has been found to enhance the stratocumulus cover and a cold SST meander has produced a cloud hole.

To corroborate the satellite studies on low-level cloud dynamics introduced above and provide more detailed continuous in situ observations, the ElUcidating the RolE of Cloud-Circulation Coupling in ClimAte (EUREC^{4}A) field campaign (Stevens et al., 2021) took place in the north-western tropical Atlantic between January and

21698996, 2022, 21, Downloaded from https://agupubs.onlinelibrary.wiley.com/doi/10.1029/2022JD036799 by Cochrane France, Wiley Online Library on [02/12/2022]. See the Terms and Conditions (https://onlinelibrary.wiley.com/terms-and-conditions) on Wiley Online Library for rules of use; OA articles are governed by the applicable Creative Commons License

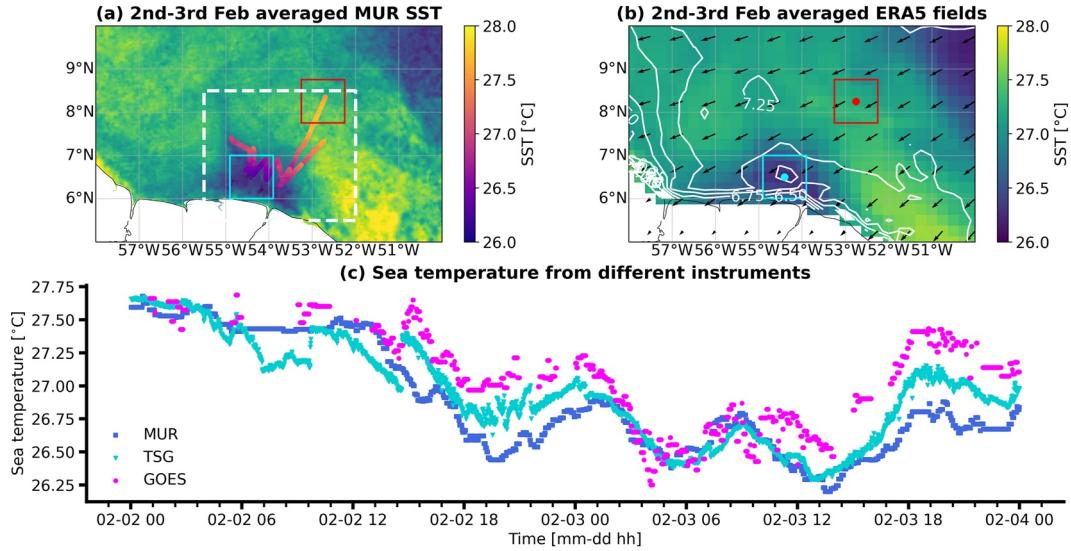


Figure 1. (a) Map of the Multi-scale Ultra-high Resolution (MUR) sea surface temperature (SST) displaying the cold patch signature averaged on the 2nd and 3rd of February 2020 together with the two R/V trajectories displaying their thermosalinograph (TSG, see the main text for details) sea temperature (with the colorbar of panel (a)), between 00:00 UTC 2nd and 00:00 UTC 4th of February 2020. The white dashed rectangle indicates where the satellite-derived cloud fields are analyzed. The cyan and the red squares shown in both panels are used for the ERA5 analyses to evaluate the large-scale signals and variability, as described in the main text. (b) Two-day averaged ERA5 fields of SST (in colors), wind speed (white contours), and wind field (arrows, sub-sampled for the sake of clarity). Note that the colorbar for the MUR and the ERA5 SST fields is the same and is shown in panel (b) only. (c) Time series of the sea temperature from the in situ TSG measurement of R/V Maria Sibylla Merian and the remotely sensed MUR and GOES products.

February 2020. The aim of the campaign was to quantify the micro- and macro-physical cloud properties as a function of the large-scale environment. Since in situ observations of air-sea interactions and their effects on the lower atmosphere are rare (especially in the tropical and sub-tropical oceans), the EUREC^{4}A-Ocean Atmosphere (OA) dedicated experiment was added to the EUREC^{4}A initial framework. The EUREC^{4}A-OA project secured the funding for two research vessels (R/Vs) during the main field campaign, with the goal of better investigating the upper ocean and lower atmosphere dynamics in an eddy-rich region between Barbados and the coasts of South America, the so-called "Boulevard des tourbillons." In particular, observations of the upper ocean stratification (modified by the large freshwater river outflow of the region), of the large eddies shedded by the North Brazilian Current (NBC) and of the lower atmospheric dynamics were sought in order to better characterize their role in the complex air-sea exchanges of the region.

Stephan et al. (2021) document an intensive observation period (IOP) during the EUREC^{4}A campaign, with a high number of radiosonde (RS) launches performed from the R/V L'Atalante. This IOP aimed to obtain detailed information on the ABL dynamics near the edge and over a remarkable surface cold patch (located between 6.3 and 7.8°N and −52.5 and −54.5°W, as shown in Figure 1a). The origin of the surface cold patch is likely coastal upwelling that is a result of a big NBC eddy sitting offshore and exporting water from the continental shelf (Reverdin et al., 2021). The R/V L'Atalante and the R/V Maria Sibylla Merian (MS Merian hereafter) sampled the cold patch between the 2nd and the 3rd of February 2020. Figure 1a shows the gap-free daily maps, representative of the foundation (night-time) conditions at 0.01° grid spacing, from the Multi-scale Ultra-high Resolution (MUR) product (JPL MUR MEaSUREs Project, 2015, (Chin et al., 2017)) averaged between the 2nd and 3rd of February 2020. The MUR product is an analysis product, provided on a daily basis, that combines different satellite (infrared at high and medium resolutions and microwave products) and in situ data (Chin et al., 2017). The MUR foundation SST map is shown together with the ship-based thermosalinograph (TSG) bulk SST measurements (introduced in details in the next section), and some areas that are used in the following analysis. The time series of the bulk SST from the TSG, the foundation SST from MUR and the skin SST from the GOES-East satellite are also shown in panel (c). The SST product from the GOES-East satellite is calibrated with bulk SST measurements but it includes the spatial and temporal variability of the skin SST (Ignatov, 2010). It is available at https://www.ncei.noaa.gov/products/satellite/goes-r-series with hourly frequency and roughly 2 km grid spacing.

21698996, 2022, 21, Downloaded from https://agupubs.onlinelibrary.wiley.com/doi/10.1029/2022JD036799 by Cochrane France, Wiley Online Library on [02/12/2022]. See the Terms and Conditions (https://onlinelibrary.wiley.com/terms-and-conditions) on Wiley Online Library for rules of use; OA articles are governed by the applicable Creative Commons License

21698996, 2022, 21, Downloaded from https://agupubs.onlinelibrary.wiley.com/doi/10.1029/2022JD036799 by Cochrane France, Wiley Online Library on [02/12/2022]. See the Terms and Conditions (https://onlinelibrary.wiley.com/terms-and-conditions) on Wiley Online Library for rules of use; OA articles are governed by the applicable Creative Commons License

The time series of the MUR and the GOES products are reconstructed with the satellite values closest to the R/V MS Merian position for each instant. This shows that the bulk SST measurements of the TSG well captures the spatial variability of the cold patch, in agreement with both satellite products. The differences among the three instruments are due to the diurnal warming.

A wide range of instruments installed on both R/Vs, including a Raman lidar, a W-band cloud radar, a micro-rain radar, and 2 Doppler lidars (DLs), were continuously operated in this area to provide ship-based remote sensing profile observations of the ABL structure and clouds. For the first time, the EUREC^4-OA framework of ship-based observations allows the investigation of small-scale processes, O(1–100) km, at open-sea in detail, exploiting the deployed instruments' unprecedented vertical and temporal resolution and the unique instruments' synergy. We undertake a multi-sensor and multi-scale analysis based on all the observations collected by the different platforms to characterize the impact of the cold SST patch on the ABL. In particular, the wind, air temperature, and humidity field responses to the SST field are linked to the observed modulation of the cloud field (in terms of vertical structure, physical, and optical properties). The physical mechanisms described above are used to interpret the dynamics. In Section 2 we describe the data and the methods used in the analysis. In Section 3 we display the main results, that are extensively discussed in Section 4 by using selected satellite products. Section 5 contains the concluding remarks.

2. Data and Methods

Here, we introduce the observations collected from the different platforms used to investigate the atmospheric impact of the cold patch. The time frame of interest is between 00:00 UTC on the 2nd and 00:00 UTC on the 4th of February 2022 (Figures 2 and 3 for monitoring data availability). We applied the following methodology to post-process the data in order to extract the atmospheric response signal to the sampled SST structure. This assumes that the cold patch does not significantly evolve in the time frame of interest (it lasts for at least a week, not shown). We calculate the diurnal cycle (DC) of all atmospheric properties (when possible and meaningful) by averaging variables every 15 min (30 min for the surface fluxes) at the same time of the day. To do this we use all the available data from the 28th of January to the 4th of February 2020, which corresponds to the R/V MS Merian navigating below 10°N. We obtain in this way a vertical-time section of each variable that is representative of its diurnal variability in this region. After interpolating it back to the original time axis of each variable, we compute the diurnal anomaly as the difference between the original data and the DC. Finally, we interpolate the anomalies to a common time coordinate and we average them over bins of SST values with an equal bin-width of 0.25 K for RSs and of 0.05 K for lidar data.

To better isolate the atmospheric response to SST, we remove the profiles in which precipitation reaches the surface using the cloud radar data (described in Section 2.4). We classify and exclude as rainy profiles those corresponding to the instants in which the lowest value of radar reflectivity above the radar sensitivity is below 300 m. The number of profiles excluded depends on the time resolution of the data set.

We exploit ERA5 reanalysis fields (Hersbach et al., 2020) to estimate the contribution of the large-scale dynamics to the observed variations. In this way, we can assess the confidence of the relationship between the observed atmospheric response and the local SST forcing. The approach adopted slightly differs for specific observations, and the subsections dedicated to those observations will provide detailed information.

2.1. Ship-Based Surface Measurements

On the R/V MS Merian, an SBE38 TSG recorded water temperature and salinity at 6.5 m below sea level with a 1-min sampling rate. Similarly, an automatic weather station was operating with various instruments to record the state of the lower atmosphere. The sensors above the average waterline at 19.88 m recorded air temperature (T) and RH every 2 s. An anemometer measured wind speed and direction from the uppermost mast at 28.7 m above the waterline with a 1 s time resolution. The pressure was recorded at 15 m above the waterline every 10 s. On the R/V L'Atalante (refer to Speich (2020) for more information regarding the campaign of this R/V), an SBE38 TSG measured the upper ocean temperature and salinity at 5 m depth from the ocean surface with a time step of 30 s. Note that the nominal depth of the measurements may not correspond to the real depth of the measurements because of the flow distortion induced by the R/Vs themselves. Figure 2a shows the time series of the TSG water temperature from both R/Vs for the time period of interest.

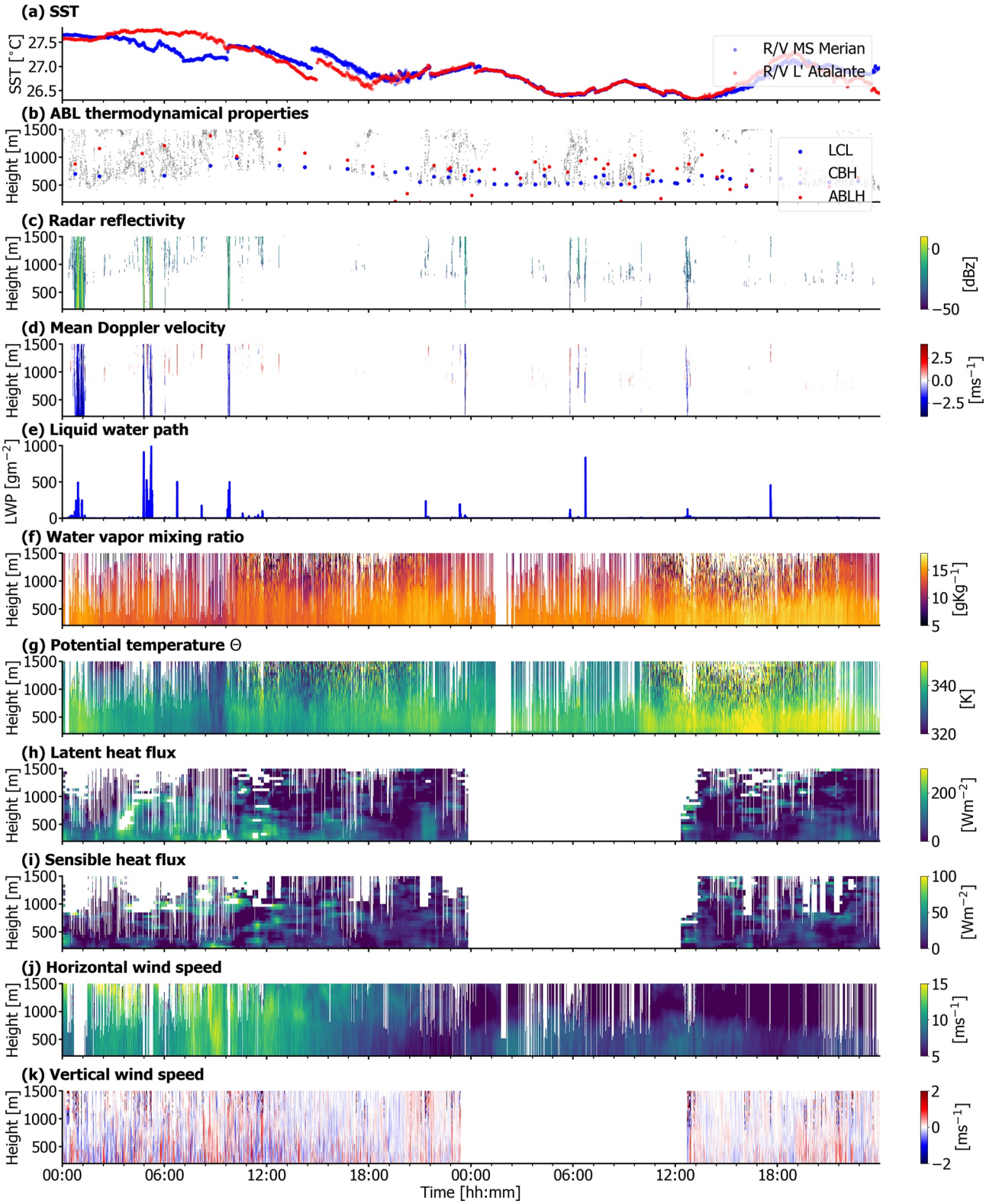


Figure 2. Time series and time-height series of the variables measured by the ship-borne instruments described in the main text.

21698996, 2022, 21, Downloaded from https://agupubs.onlinelibrary.wiley.com/doi/10.1029/2022JD036799 by Cochrane France, Wiley Online Library on [02/12/2022]. See the Terms and Conditions (https://onlinelibrary.wiley.com/terms-and-conditions) on Wiley Online Library for rules of use; OA articles are governed by the applicable Creative Commons License

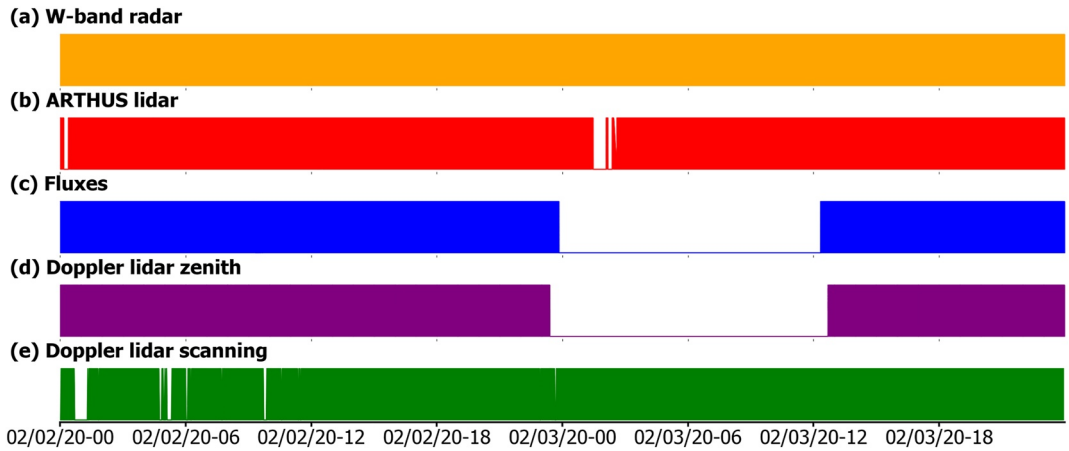


Figure 3. Data availability of the measurements from the ship-borne instruments considered in this work: colored bars denote that data are available.

Romps (2017) calculates the lifting condensation level (LCL), that is, the height at which the surface air parcel reaches saturation based on surface pressure, RH, and temperature. We follow Romps (2017) approach to compute the LCL time series with the weather station surface data collected on the R/V MS Merian, at the instants when RSs are launched, as in Figure 2b (in blue).

2.2. Radiosondes

Stephan et al. (2021) describe the RSs data set launched from the R/V L'Atalante and the R/V MS Merian, together with those launched from two more R/Vs and the Barbados Cloud Observatory. Between the 2nd and the 3rd of February, 2 RSs were launched from the R/V MS Merian, while from the R/V L'Atalante 28 Meteomodem RSs and 23 Vaisala RSs (51 in total) were launched. The preliminary analysis of the atmospheric response to the mesoscale cold patch presented in Stephan et al. (2021) is brought here to deeper detail.

To analyze the vertical atmospheric structure as a function of the SST, we bin the R/V MS Merian TSG SST with bins of 0.25°C. Then, we assign the closest SST measurement to each RS launch, and group the RSs over the same SST bins.

The ABL height (ABLH) can be computed from RS data with different methods. We consider the bulk Richardson number (Ri_B) method, initially proposed by Vogelezang and Holtslag (1996). For a given height z, $\mathrm{Ri}_B(z)$ is defined as the ratio between the turbulence associated with the buoyancy and the turbulence induced by the mechanical shear, namely, following Seidel et al. (2012),

$$\mathrm{Ri}_B(z) = \frac{(g/\theta_{vs})(\theta_{vz} - \theta_{vs})(z - z_s)}{(u_z - u_s)^2 + (v_z - v_s)^2 + \left(bu_*^2\right)} \tag{1}$$

where the subscript s indicates surface properties, g is the acceleration due to gravity, θ_v is the virtual potential temperature, b is a constant, u_* is the friction velocity, and u and v are the zonal and meridional wind speeds. In this work, we assume $b = 0$, ignoring the surface frictional effects, and we compute the surface properties using the ship measurements (as described in Section 2.1). The ABLH is the lowest height where $\mathrm{Ri}_B(z)$ exceeds the value of 0.25 (Davison et al., 2013; Seidel et al., 2012). Figure 2b shows (in red) the time series of the ABLH derived from the RS observations.

2.3. Raman Lidar and Doppler Lidars

The Atmospheric Raman Temperature and Humidity Sounder (ARTHUS, Lange et al., 2019) was operated on the R/V MS Merian to retrieve water-vapor mixing ratio (WVMR), temperature (T), and aerosol profiles with unprecedented vertical resolution of 7.5 m and 10 s in the lower troposphere. The lidar laser source is a injection-seeded Nd: YAG laser, where only the third harmonic is transmitted into the atmosphere (354.83 nm).

21698996, 2022, 21, Downloaded from https://agupubs.onlinelibrary.wiley.com/doi/10.1029/2022JD036799 by Cochrane France, Wiley Online Library on [02/12/2022]. See the Terms and Conditions (https://onlinelibrary.wiley.com/terms-and-conditions) on Wiley Online Library for rules of use; OA articles are governed by the applicable Creative Commons License

21698996, 2022, 21, Downloaded from https://agupubs.onlinelibrary.wiley.com/doi/10.1029/2022JD036799 by Cochrane France, Wiley Online Library on [02/12/2022]. See the Terms and Conditions (https://onlinelibrary.wiley.com/terms-and-conditions) on Wiley Online Library for rules of use; OA articles are governed by the applicable Creative Commons License

ARTHUS was designed in such a way that is already eye-safe when the laser beam leaves the housing. Profiles of WVMR are obtained combining a WV Raman backscatter signal by the temperature-independent combination of two (high and low) rotational Raman signals. On the other hand, the T profiles are obtained calibrating the ratio of the high to low rotational Raman signals.

Two DLs on the R/V MS Merian measured the wind field. Both DLs were Streamline XR from HALO Photonics (Pearson et al., 2009) at 1.5 μm wavelength, with a pulse repetition frequency of 10 kHz. One DL operated in vertical staring mode to retrieve vertical wind velocity next to ARTHUS. The other DL operated in a 6-beam Velocity Azimuth Display (VAD) mode to measure the horizontal wind velocity. In particular, a scan pattern in step and stare mode was programmed with five beams pointing to azimuth angles of 0°, 72°, 144°, 216°, and 288°, with a 45° elevation angle. The sixth beam pointed vertically. In each direction, 10 profiles were recorded. The range resolution of the two DLs is 30 m with a temporal integration time of 1 s for the vertical staring DL, and 20 m with a time step of 90 s in the VAD mode. The nominal measurement range is 10 km (vertical staring mode) and 12 km (6-beam VAD mode), but the useable data depends on scatterers' presence in the atmosphere. In particular, the presence of clouds stops reliable measurements, as described below.

The method introduced in Lenschow et al. (2000) and refined in Wulfmeyer et al. (2016) allows to resolve the turbulent moments of T, WVMR, and vertical wind. Therefore, instrument noise uncertainties can be estimated. The sensible and latent heat fluxes (SHF and LHF) profiles were calculated using the eddy covariance method described in Wulfmeyer et al. (2016), as applied, for example, in Behrendt et al. (2020). The T, WVMR, vertical wind, SHF, and LHF used in this paper, have a temporal resolution of 60 min, shifted by a 10 min step (therefore, one profile every 10 min is available). Their range resolution is 50 m. The instrumental uncertainties in the ABL are 0.2 K for T, 0.1 g kg^{-1} for WVMR, 0.3 m s^{-1} for vertical wind speed, and 0.5 m s^{-1} for horizontal wind speed.

The entire data set collected during the EUREC^{4}A campaign by the ARTHUS and the DLs will be presented in a future dedicated publication. Figures 2f–2k show the height-time sections of the variables measured by ARTHUS and the DLs. Note that potential temperature (panel g) is computed from the ARTHUS temperature profiles T following its standard definition and using a hydrostatic pressure profile derived from the surface pressure measurement of the R/V MS Merian weather station.

To reduce the noise, we apply some pre-processing steps before analyzing the data as a function of the SST forcing. First, all variables are averaged over 10 s intervals to reduce the ship motion effects. Second, we remove all values outside reasonable ranges. The selected valid ranges for the different variables are: from 0 to 20 g kg^{-1} for WVMR, from 270 to 310 K for T, from −5 to 5 m s^{-1} for vertical wind velocity, from 0 to 20 m s^{-1} for horizontal wind velocity, from −250 to 250 W m^{-2} for LHF, and from −100 to 100 W m^{-2} for SHF. Given that T decreases with height, its valid range only applies between 200 and 3,000 m. Third, we define the cloud base height (CBH) (Figure 2b in gray) as 100 m (experimental value adopted by the authors) below the altitude where the largest vertical gradient in the backscatter ratio occurs. This follows the method in Wang and Sassen (2001), as there is no widely accepted method to detect the cloud base using lidars. This values of CBH are used to mask out the ARTHUS and DLs observations, as they are known not to be reliable within the clouds (Lange et al., 2019).

The post-processing described above is applied to the vertical profiles of WVMR, T, vertical and horizontal wind speed, SHF, and LHF. The width of the SST bins used to average the rain-free diurnal anomalies of ARTHUS- and DL-derived observations is chosen as follows. On the one hand we want to keep the high resolution of the data. On the other hand, we aim to have enough values per bin (roughly 200) to reduce the noise and detect a significant signal. The selected bin width is 0.05°C. For each SST bin, we compute the mean and standard deviation profiles. In this way, all consecutive mean profiles compose a vertical-SST section of the diurnal anomalies. The uncertainties estimated from their instrumental values and the setup of the instruments are: 1.5 K for potential temperature, 1 g kg^{-1} for WVMR, 0.3 m s^{-1} for vertical wind speed, 1 m s^{-1} for horizontal wind speed, and 50 W m^{-2} for surface turbulent heat fluxes. They are propagated in the computations of the height-SST sections to evaluate when the signal is significant, as explained in Appendix A.

We also compare the distributions of the vertical wind velocities for the top and lowest deciles of TSG SST (26.4°C and 27.5°C, respectively) to examine the atmospheric states on the extreme SST forcing of the case study. Since the vertical velocity data have a gap during the analyzed period, the total number of occurrences for the 10th and the 90th SST percentiles are different (with 24,688 and 22,784 values, respectively, as indicated in the legend of Figure 5a).

21698996, 2022, 21, Downloaded from https://agupubs.onlinelibrary.wiley.com/doi/10.1029/2022JD036799 by Cochrane France, Wiley Online Library on [02/12/2022]. See the Terms and Conditions (https://onlinelibrary.wiley.com/terms-and-conditions) on Wiley Online Library for rules of use; OA articles are governed by the applicable Creative Commons License

2.4. W-Band Cloud Radar

The W-band radar deployed on the R/V MS Merian is a frequency-modulated continuous-wave 94 GHz dual-polarization radar equipped with a radiometric channel at 89 GHz. It is manufactured by Radiometer Physics GmbH in Germany. Küchler et al. (2017) provide a detailed description of the instrument. The radar reflectivity factor (Ze, reflectivity from now on) and the mean Doppler velocity (Vd) are sampled with a 3 s time resolution. The vertical resolution is 7.5 m between 100 and 1,233 m, 9.2 m between 1,233 and 3,000 m, and 34.1 m between 3,000 and 10,000 m. The radar stands on a stabilization platform to reduce the impact of ship motions on its Doppler measurements. Acquistapace, Coulter, et al. (2022) report a detailed description of the impact of the stabilization on the data, the setup used on the ship, and the details on the retrieval for the liquid water path (LWP). Time series of reflectivity, mean Doppler velocity and LWP are shown in Figures 2c–2e.

For the radar data, we verify that there is no DC of cumulus clouds between the 28th and 4th of February 2020. Thus, we directly use the radar variables instead of their daily anomalies. We separate rainy from non-rainy profiles using the same criterion explained in the previous subsection (when a non-zero reflectivity is detected below cloud base the profile is considered to be rainy), and we develop most of the analysis looking at the non-rainy profiles. We calculate the hydrometeor fraction from the radar reflectivity using a 15 min time resolution. We then bin the radar reflectivity, the mean Doppler velocity (Vd), LWP, and the cloud fraction for the corresponding R/V MS Merian TSG SST. Mean and standard deviation profiles for the hydrometeor fraction, mean LWP versus SST bins, and 2D histograms of Ze and Vd occurrences as a function of height for each SST bin are computed.

2.5. Reanalysis Data

We use reanalysis data to estimate the extent to which the large-scale variability in the 2 days of interest masks or affects the in situ observed atmospheric response to the SST forcing. Ship-borne instruments record the atmospheric variations due to the differential surface thermal forcing and the temporal variability controlled by, for example, the DC and the large-scale dynamics. From reanalysis data, instead, the temporal variability signal can be isolated, as described below.

We extract hourly ERA5 gridded fields (available at https://cds.climate.copernicus.eu/cdsapp%23%21/dataset/reanalysis%2Dera5%2Dpressure%2Dlevels%3Ftab%3Dform, last accessed March 2022) of the following variables: SST, LHF, ABLH, CBH, 2 m air temperature, 2 m dewpoint temperature, 10 horizontal wind components, water vapor mixing ratio, air temperature, and horizontal wind components. They are retrieved between the surface and 700 hPa in the time frame of interest (between 00:00 UTC 2nd and 00:00 UTC 4th February 2020). The ERA5 2-day averaged SST (Figure 1b) appears to be smoother, as expected, than the corresponding 2-day averaged MUR SST (Figure 1a). Most RS profiles measured from the R/V L'Atalante during the campaign (114 out of 186, none from the R/V MS Merian) were sent to the European Centre for Medium-range Weather Forecasts for assimilation in ERA5 (Stephan et al., 2021). Even if Savazzi et al. (2022) showed that the assimilation of RS data is negligible on the wind field, the reanalysis fields should not be considered as independent data but as a physically based spatio-temporal interpolation of the observations. Reanalysis data can be used to estimate the large-scale variability signal to isolate the local one better. We compute the time-height sections of air temperature, specific humidity, and wind speed and direction by spatially averaging the fields over the white dashed rectangle of Figure 1a to characterize the synoptic evolution in the time frame of interest. Also, the time series of the surface variables (LHF, CBH, ABLH, 2 m temperature and humidity, and 10 m horizontal wind speed), averaged over the same area, allow an estimate the synoptic scale signal (Figure S1 in Supporting Information S1).

We also consider the instantaneous vertical profiles corresponding to two instants when the R/V L'Atalante was in the warm and cold side of the oceanic structure. The "warm" point is at 52.75°W and 8.25°N and the "cold" point is at 54.4°W and 6.5°N. In both points, two profiles are extracted at different times: at 00:00 UTC on the 2nd of February and at 06:00 UTC on the 3rd of February. These correspond, respectively, to the instants when the R/V L'Atalante was in the warm and the cold points. Thus, the profile extracted on the warm point on the 2nd of February and the profile extracted on the cold point on the 3rd of February can be directly compared with the RS data. We select an area of $1° \times 1°$ around these positions to compute the mean profiles to avoid relying on a single model point (Figure 1). The added value of considering two instants in both points is that the comparison between the profiles extracted in the same location is indicative of the large-scale dynamics. In addition, we also

21698996, 2022, 21, Downloaded from https://agupubs.onlinelibrary.wiley.com/doi/10.1029/2022JD036799 by Cochrane France, Wiley Online Library on [02/12/2022]. See the Terms and Conditions (https://onlinelibrary.wiley.com/terms-and-conditions) on Wiley Online Library for rules of use; OA articles are governed by the applicable Creative Commons License

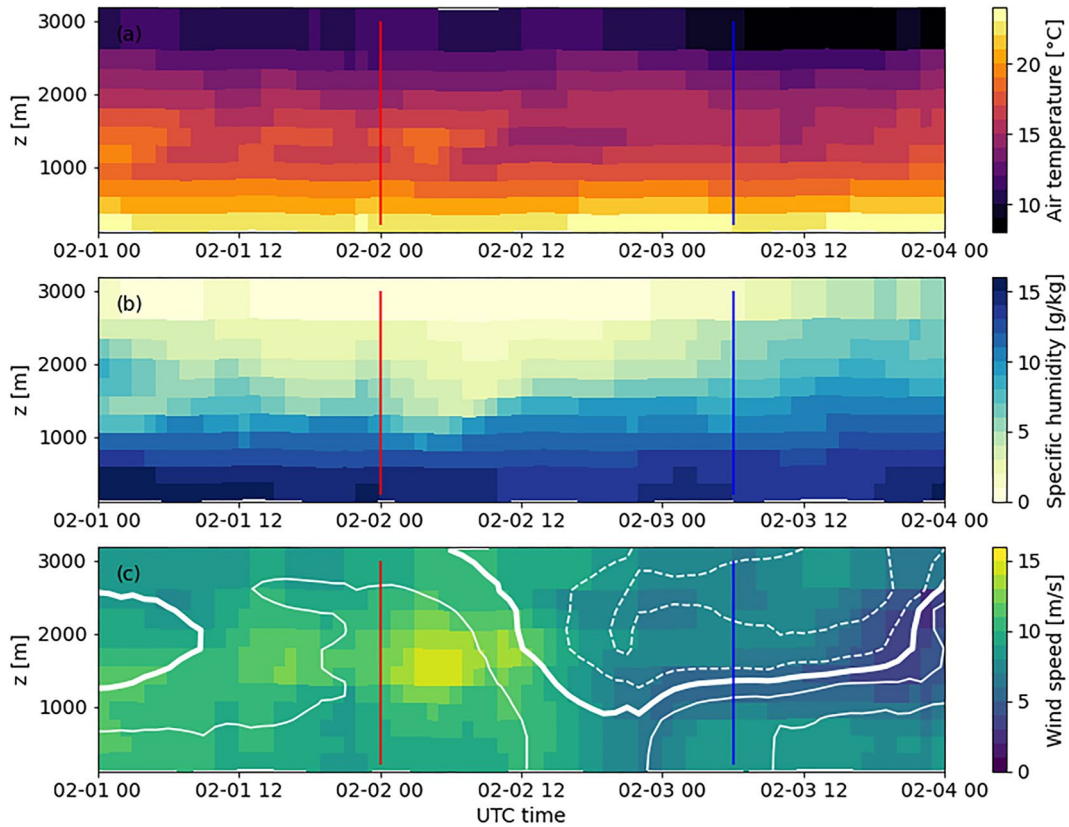


Figure 4. Time-height sections between 00:00 UTC of the 1st and 00:00 UTC of the 4th of February 2020 of (a) air temperature, (b) specific humidity, and (c) wind speed (color) and direction (contour). The fields are spatially averaged on the area denoted with the white dashed rectangle in Figure 1a. The wind direction is defined to be positive counterclockwise from east. Contour lines are drawn every 20°, with positive and negative values indicated by solid and dashed lines, respectively. The zero-degree line (corresponding to winds blowing from East) is solid thick. The vertical red and blue lines correspond to the "warm" and "cold" points introduced in the main text.

compute the mean, and standard deviation profiles over the 2 days of interest, separating the cold and the warm points. These temporal statistics are useful (a) to evaluate how ERA5 captures the mean difference due to the surface thermal forcing and (b) to compare it with the temporal variability induced by the large-scale dynamics.

3. Results

The analysis of the atmospheric response to the cold mesoscale structure covers the time frame between 00:00 UTC 2nd and 00:00 UTC 4th of February 2020, when the R/V L'Atalante and the R/V MS Merian sampled the SST forcing of interest together. Over the cold patch (Figure 1a), we observe the trades' typical surface north-easterly wind flow in this season (Figure 1b). The averaged wind speed is relatively homogeneous, with a band of low wind speed close to the coastline likely due to the daily air-sea breeze system.

We consider hourly ERA5 data to characterize the synoptic evolution between the 1st and the 3rd of February. In particular, we look at time-height sections obtained by spatially averaging over the area denoted with the white dashed rectangle in Figure 1a (Figure 4). The reanalysis indicates that in the morning of the 2nd of February a relatively warm and dry air mass, characterized by strong wind speed, arrived from east-north-east between 1,000 and 2,000 m. At around 12:00 UTC on the 2nd of February, the wind above 1,000 m changed direction by roughly 40° in 6 hr, coinciding with a more humid and slightly cooler air mass (coming from east-south-east). A layer of weak wind speed developed between the surface air mass and the one above 1,000 m. Below 1,000 m, the area-averaged changes in wind speed are weaker, with an oscillation of roughly 4 m s^{-1} amplitude around 14:00 UTC on the 2nd of February. The diurnal warming and moistening signals appear in the lowest model level, with a slight drying of about 1 g kg^{-1} in the sub-cloud layer at around 12:00 UTC on the 2nd of February.

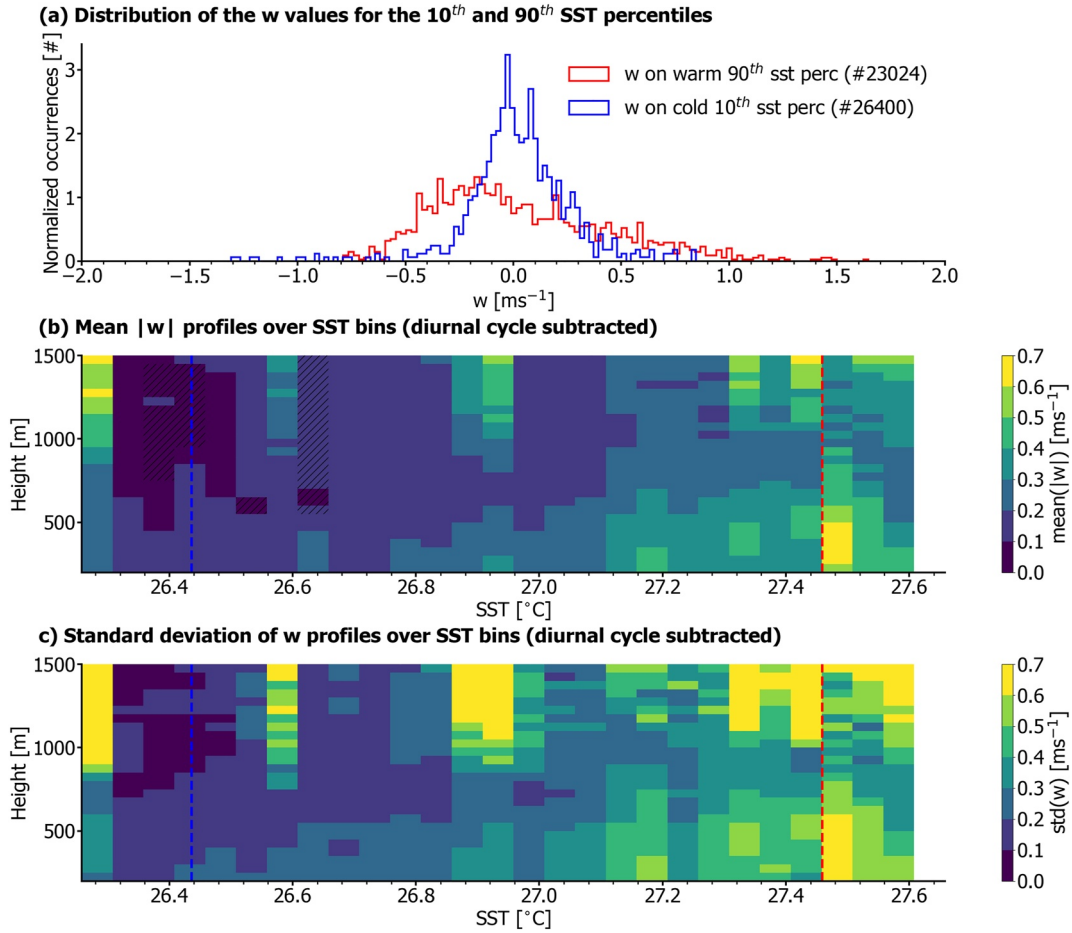


Figure 5. (a) Conditional distributions of vertical velocity *w*, from the vertical staring Doppler lidar, over the warmest thermosalinograph (TSG) sea surface temperature (SST) decile (red curve) and the coolest TSG SST decile (blue curve). Such deciles are shown as vertical dashed lines in panels (b and c), and the *w* data between 200 and 750 m are used. (b, c) show the mean absolute value and the standard deviation of rain-free daily anomaly of *w* as a function of the height and the SST.

The warm SST region displays a vigorous mixing of the vertical wind velocity anomaly obtained from vertical staring DL data (Figure 5b) that is not present on the cold SST waters. In particular, considering the sub-cloud layer (roughly below 750 m), absolute values of mean vertical velocity are larger over the warm SST than the cold patch. Also the standard deviation signal, shown in Figure 5c, indicates that more substantial vertical fluctuations occur over warmer waters. We derived the rain-free diurnal anomaly vertical wind velocity distributions by considering all the available points between 200 and 700 m and by separating them below the coolest TSG sea temperature decile and above the warmest TSG sea temperature decile (Figure 5a). The distribution over the warm decile is much wider than the distribution over the cold decile. In fact, the standard deviation over the cold decile is 0.5 m s^{-1}, compared to the warm decile's one of 0.2 m s^{-1}. This confirms that vertical velocity fluctuations are stronger over the warm SST, in agreement with past observational data (Skyllingstad et al., 2007) and recent LES modeling findings (Sullivan et al., 2020).

Horizontal wind speed measurements from all instruments, derived from the VAD scanning DL (Figure 6d) and the RSs data (Figure 6a), detect a response in agreement with the DMM mechanism. ERA5 instantaneous profiles (Figure 6b) show that the temporal variability due to the large-scale dynamics corresponds to a significant reduction of the wind speed at the upper levels (above 750 m) and a 1 m s^{-1} reduction near the surface. Since this happens on both the warm and cold areas separately (compare the solid and the dashed lines of panel b) and corresponds to the spatially averaged signal of the synoptic dynamics (as in Figure 4c), we claim that it is not due to the SST spatial variability. In ERA5, thus, there seems not to be a signal due to the surface forcing. This is

21698996, 2022, 21, Downloaded from https://agupubs.onlinelibrary.wiley.com/doi/10.1029/2022JD036799 by Cochrane France, Wiley Online Library on [02/12/2022]. See the Terms and Conditions (https://onlinelibrary.wiley.com/terms-and-conditions) on Wiley Online Library for rules of use; OA articles are governed by the applicable Creative Commons License

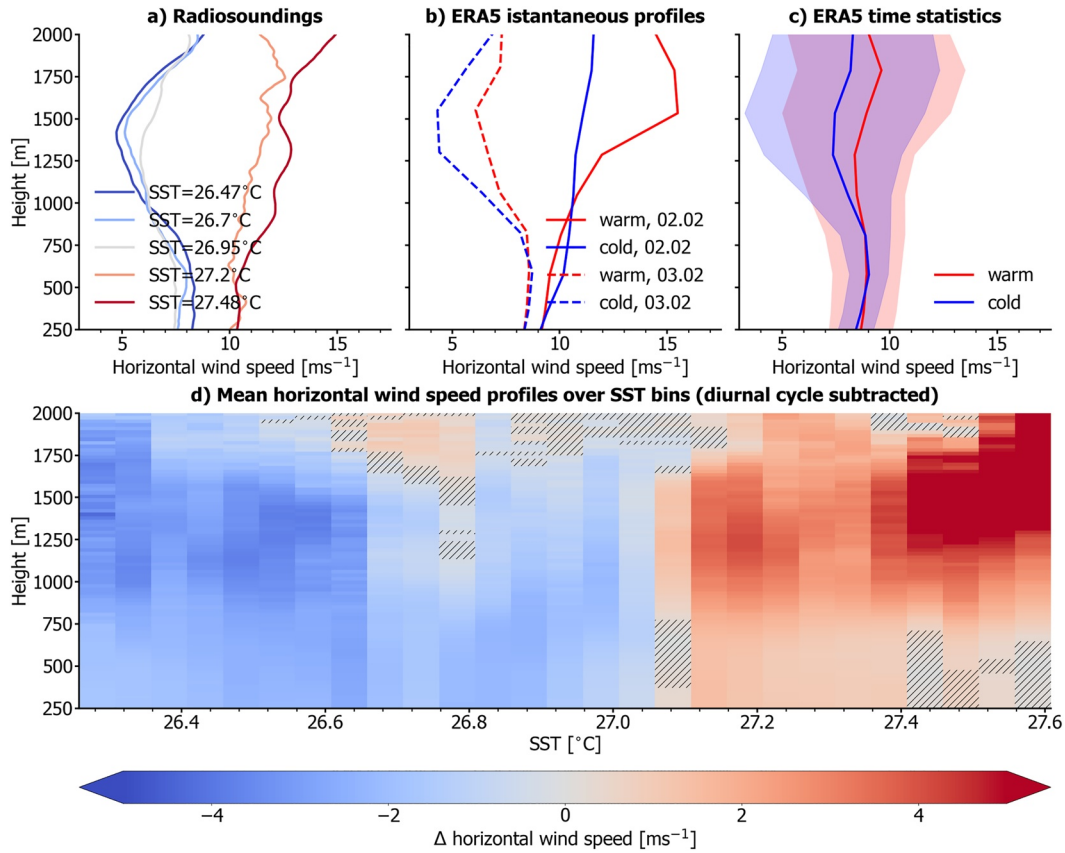


Figure 6. Horizontal wind: (a) radiosonde profiles binned on the thermosalinograph sea surface temperature (SST), (b) instantaneous, and (c) 2-day averaged ERA5 profiles over the warm and cold boxes of Figure 1d Doppler lidar-derived rain-free daily anomaly as a function of SST and height. Hatched pixels are not significantly different from 0.

confirmed by the fact that the 2-day averaged vertical profiles over the cold and the warm areas have a zero mean difference in the sub-cloud layer and a small difference (compared to the temporal standard deviation) above 750 m (panel c). Note that Savazzi et al. (2022) highlight and deeply investigate the wind biases between ERA and the RS data during the EUREC^4 campaign. Despite such biases, however, we consider the ERA5 information to be reliable because it is extracted as a temporal or spatial variation.

The binned RS profiles detect a reduction of wind speed of about 3–4 m s^{-1} near the surface (panel a), which is larger than the temporal variability estimated with ERA5 of about 1 m s^{-1} (confirmed in Figure S1 in Supporting Information S1). Thus, RSs data indicate a stronger reduction in the surface wind field with respect to the large-scale temporal variability, suggesting a possible local effect due to the colder SST. The height-SST section of DL-derived rain-free daily anomaly of horizontal wind speed shown in panel (d) confirms that the in situ observations detect a reduction of surface wind speed around 3 m s^{-1}, that is larger than the signal induced by the large-scale dynamics, and is in agreement with the DMM mechanism. For the horizontal wind speed, the assumed measurement uncertainty of 1 ms^{-1} and the error propagation result in the hatching of some measurement areas. Such areas are considered non-significant because the anomaly is within 3 standard deviations from zero.

We investigate the patterns in potential temperature θ using RSs, ARTHUS, and ERA5 data. RS measurements suggest a change in the lowest inversion layer, with the uniform θ layer being thicker over warmer SST, also confirmed by the ERA5 averaged profiles. However, the detailed analysis using the height-SST section of ARTHUS-derived rain-free daily anomaly does not reveal a substantial signature in θ profiles that can be ascribed to the different SST forcing (not shown). Such a weak thermal atmospheric response could be linked to a non-significant SHF pattern as a function of the SST, as discussed below.

21698996, 2022, 21, Downloaded from https://agupubs.onlinelibrary.wiley.com/doi/10.1029/2022JD036799 by Cochrane France, Wiley Online Library on [02/12/2022]. See the Terms and Conditions (https://onlinelibrary.wiley.com/terms-and-conditions) on Wiley Online Library for rules of use; OA articles are governed by the applicable Creative Commons License

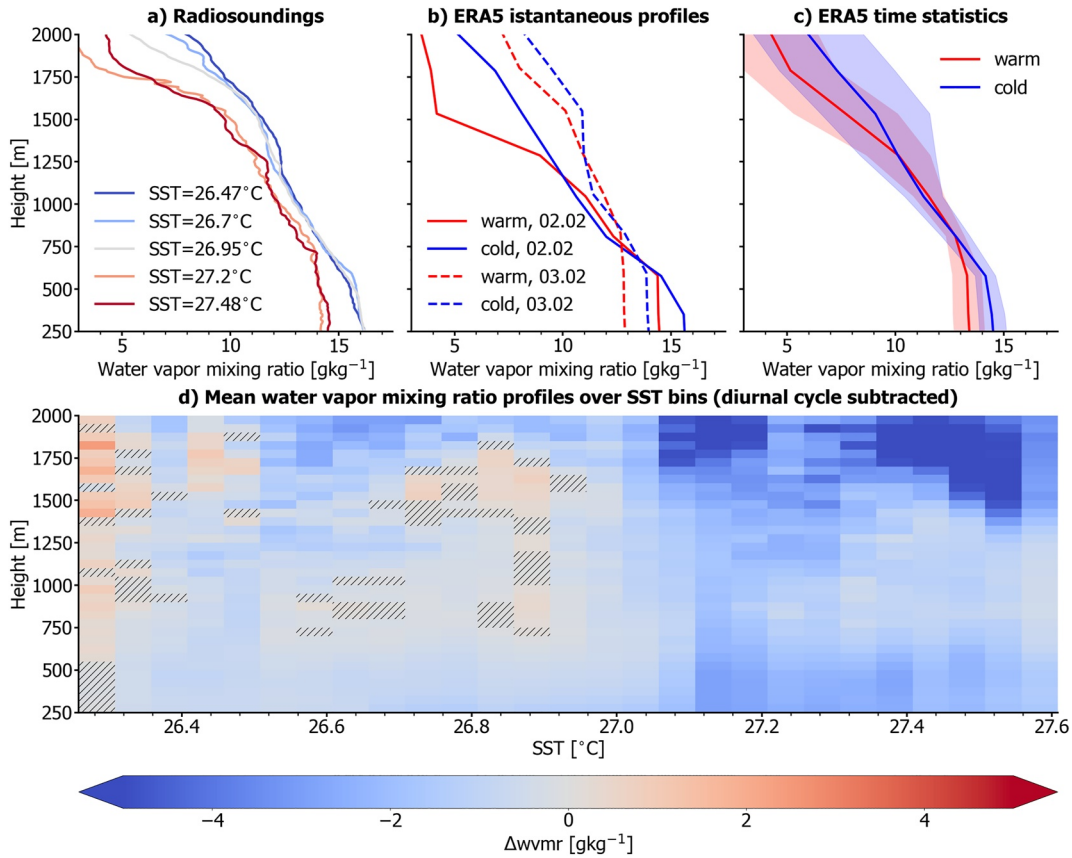


Figure 7. (a) Water-vapor mixing ratio (WVMR) radiosonde profiles binned against thermosalinograph sea surface temperature (SST), (b) instantaneous WVMR ERA5 mean profiles, and (c) 2-day mean and standard deviation WVMR ERA5 profiles computed over the warm and the cold boxes defined in the main text. (d) Height-SST section of the rain-free daily anomaly Atmospheric Raman Temperature and Humidity Sounder WVMR data.

Over the cold patch, a shallower and more humid ABL is observed in RS data (Figure 7a). The observed variation of sub-cloud layer WVMR, that includes both temporal and spatial variability, is around 2 g kg^{-1} (cold water on the 3rd of February—warm water on the 2nd of February). Stephan et al. (2021) noted that the Meteomodem RSs measured a 5% larger RH with respect to Vaisala RSs, corresponding to a WVMR bias of 1 g kg^{-1} (see Appendix B for details). In the extreme limit of considering that over the warm SST only Vaisala RSs are used and over the cold patch only Meteomodem RSs are used (more Vaisala RS are indeed launched over the warm SST, see Stephan et al. (2021)), we can state that the net observed WVMR signal is 1 g kg^{-1}.

ERA5 instantaneous profiles (Figure 7b) indicate an overall drying at the surface due to the large-scale dynamics, as the profiles on both the warm and the cold points shift by about −1.5 g kg^{-1} between the 2nd and the 3rd of February. This is also confirmed by the synoptic scale evolution shown in Figure 4b. In terms of differential SST forcing, instead, ERA5 depicts a mean increase of surface WVMR of about 1 g kg^{-1} associated with a shallower ABL over the cold water, as suggested by the temporal averaged profiles of panel (c). Thus, in the reanalysis, the combined net variation of surface WVMR between the cold water on the 3rd of February and warm water on the 2nd of February is roughly −0.5 g kg^{-1}, to be compared with the observed 1 g kg^{-1} variation. This means that when both temporal and spatial variability are accounted for, ERA5 predicts a weak drying over the cold water. Thus, at the surface, ERA5 does not fully agree with the observations. In particular, it seems that the numerical model of the reanalysis underestimates the change in stability over the cold water, producing a too weak reduction of vertical mixing. This can be ascribed to the difficulties that the ABL numerical scheme has in correctly reproducing the lower atmospheric mixing, which is likely to be responsible for the observed wind biases (Savazzi et al., 2022). Different ABL numerical schemes produce different mixing, resulting in different air-sea coupling (Perlin et al., 2014). Despite the large-scale drying, both RS and the 2-day averaged ERA5 profiles (Figure 7c)

21698996, 2022, 21, Downloaded from https://agupubs.onlinelibrary.wiley.com/doi/10.1029/2022JD036799 by Cochrane France, Wiley Online Library on [02/12/2022]. See the Terms and Conditions (https://onlinelibrary.wiley.com/terms-and-conditions) on Wiley Online Library for rules of use; OA articles are governed by the applicable Creative Commons License

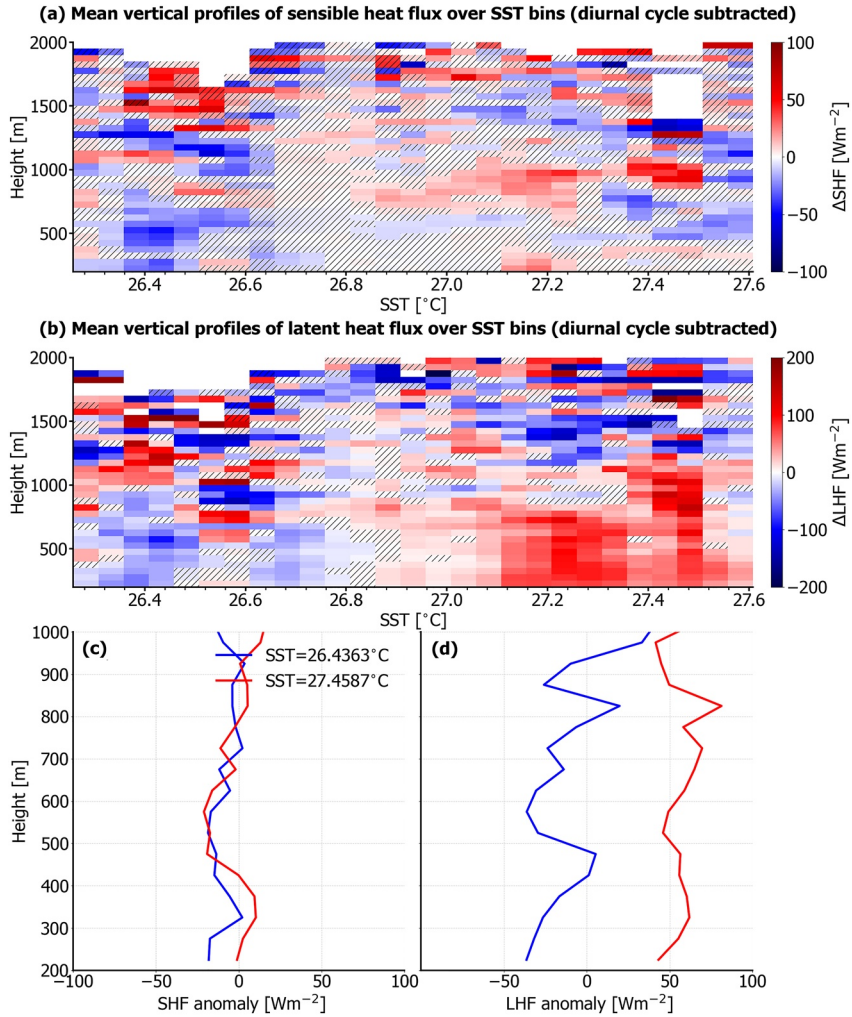


Figure 8. Height-sea surface temperature (SST) section of the rain-free diurnal anomalies of (a) sensible heat flux (SHF) and (b) latent heat flux (LHF) estimated from Atmospheric Raman Temperature and Humidity Sounder and Doppler lidars observations. Mean vertical profiles of the height-SST sections of (c) SHF and (d) LHF on the warmest and coolest SST deciles.

highlight that: (a) the surface WVMR over the cold patch is larger than over the warm SST and (b) the ABL depth, where WVMR can be considered constant with height, is reduced by more than 200 m on the cold patch compared to over the warm SST. This suggests that the local atmosphere responds to the SST structure with a shallower and more humid ABL over the cold patch, related to the weaker vertical mixing, already observed in the previous wind data (Figure 5). Also the height-SST section of ARTHUS rain-free daily anomaly of WVMR (Figure 7d) shows a net moisture excess of about 1.5 g kg^{-1} in the surface layer over the cold patch with respect to the warm waters, confirming the behavior described above.

Bulk models of trade-wind ABL dynamics (e.g., Neggers et al., 2006; Zheng, 2019) agree with a decrease of ABLH and an increase of surface WVMR over cold SST waters. In fact, in these models, the entrainment rate at the ABL top, which is the only factor that can make the ABLH grow, is proportional to the surface turbulent fluxes, which increase with increasing SST. In particular, Zheng (2019) shows that, at equilibrium, a variation of 1 K in SST corresponds to a variation of roughly 250 m for the ABLH and of roughly 2 g kg^{-1} for the WVMR, in line with the observed values.

Figure 8b shows a net positive difference of LHF between warm and cold waters that is a result of the larger wind speed (Figure 6) and the thicker mixed layer for WVMR (Figure 7), corresponding to lower surface WVMR, observed over the warm SST region. In fact, LHF scales with the wind speed and with the difference between

21698996, 2022, 21, Downloaded from https://agupubs.onlinelibrary.wiley.com/doi/10.1029/2022JD036799 by Cochrane France, Wiley Online Library on [02/12/2022]. See the Terms and Conditions (https://onlinelibrary.wiley.com/terms-and-conditions) on Wiley Online Library for rules of use; OA articles are governed by the applicable Creative Commons License

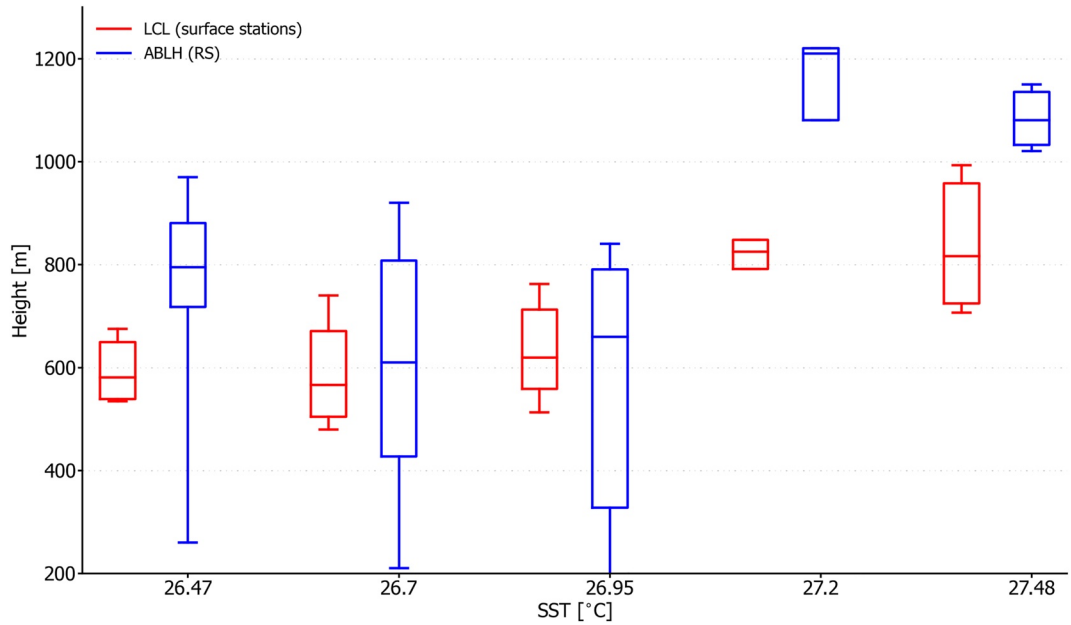


Figure 9. Box-plots of atmospheric boundary layer height (blue) and lifting condensation level (red) computed from radiosonde data binned against the thermosalinograph sea surface temperature.

saturation WVMR (that increases with increasing SST according to the Clausius-Clapeyron equation) and the actual surface WVMR. Both terms increase over the warm SST, resulting in a positive significant LHF daily anomaly, while they both decrease over the cold SST, resulting in a weaker, but still detectable, negative LHF anomaly. In terms of sensible heat flux, SHF, the results are noisier, because the uncertainty associated to the measurements ($\sigma_{LHF} = \sigma_{SHF} = 50$ W m^{-2}) is comparable to the signal itself. The mean vertical profiles of the turbulent fluxes computed over the warmest and the coolest SST deciles (panels (c) and (d)) also confirm that the LHF signal is detectable and the SHF signal is not. In particular, we can estimate that the mean LHF change in the subcloud layer (below 700 m) is roughly -70 W m^{-2} between the cold and the warm sea temperatures. The synoptic variability between the cold and the warm points estimated from ERA5 data (Figure S1 in Supporting Information S1) is $+8.5$ W m^{-2}, suggesting that the net variation is around -80 W m^{-2}.

From the instantaneous LCL and ABLH values calculated from the RS observations, one can derive their distributions based on the TSG SST bins used for the RS analyses (Figure 9). Both LCL and ABLH get higher over a warmer SST, in agreement with the signal of stronger vertical mixing detected in the wind and humidity fields. Moreover, on the cold patch ABLH and LCL have similar mean values, while over warmer waters the ABLH is, at least, 200 m higher than the LCL. This result suggests that thanks to the stronger vertical mixing detected over the warm SST, it is more likely that WVMR, temperature, and momentum are mixed above the LCL over the warm than over the cold patch area.

When WVMR is brought above the LCL it can foster the formation of liquid clouds because it increases the supersaturation and thus the diffusive droplet growth. We hypothesize that this physical mechanism can explain the higher amount of cloudiness observed over the warm water, where also stronger vertical mixing takes place. We detect more liquid water over the warm SST (Figure 10a) and the cloud vertical structure changes as a function of the underlying SST (Figures 10b and 10c).

Rain can alter the cloud macroscopic structure that radars can reveal. For this reason, we derived hydrometeor fraction profiles and Contour Frequency by Altitude Diagrams (CFADs) for radar reflectivity and mean Doppler velocity for non-rainy cloud columns only. The LWP observations in rainy condition can be biased due to the wet radome of the radar, but we retain the LWP observations also in rainy conditions because all values are much smaller than 1,000 g m^{-2}, considered as a threshold corresponding to saturation in the MWR channels (Acquistapace, Coulter, et al., 2022). Over the cold SST, the hydrometeor profile displays two main cloudy peaks, one at the LCL, around 700 m, and the second one right below the inversion height (Figure 10b). Moving

21698996, 2022, 21, Downloaded from https://agupubs.onlinelibrary.wiley.com/doi/10.1029/2022JD036799 by Cochrane France, Wiley Online Library on [02/12/2022]. See the Terms and Conditions (https://onlinelibrary.wiley.com/terms-and-conditions) on Wiley Online Library for rules of use; OA articles are governed by the applicable Creative Commons License

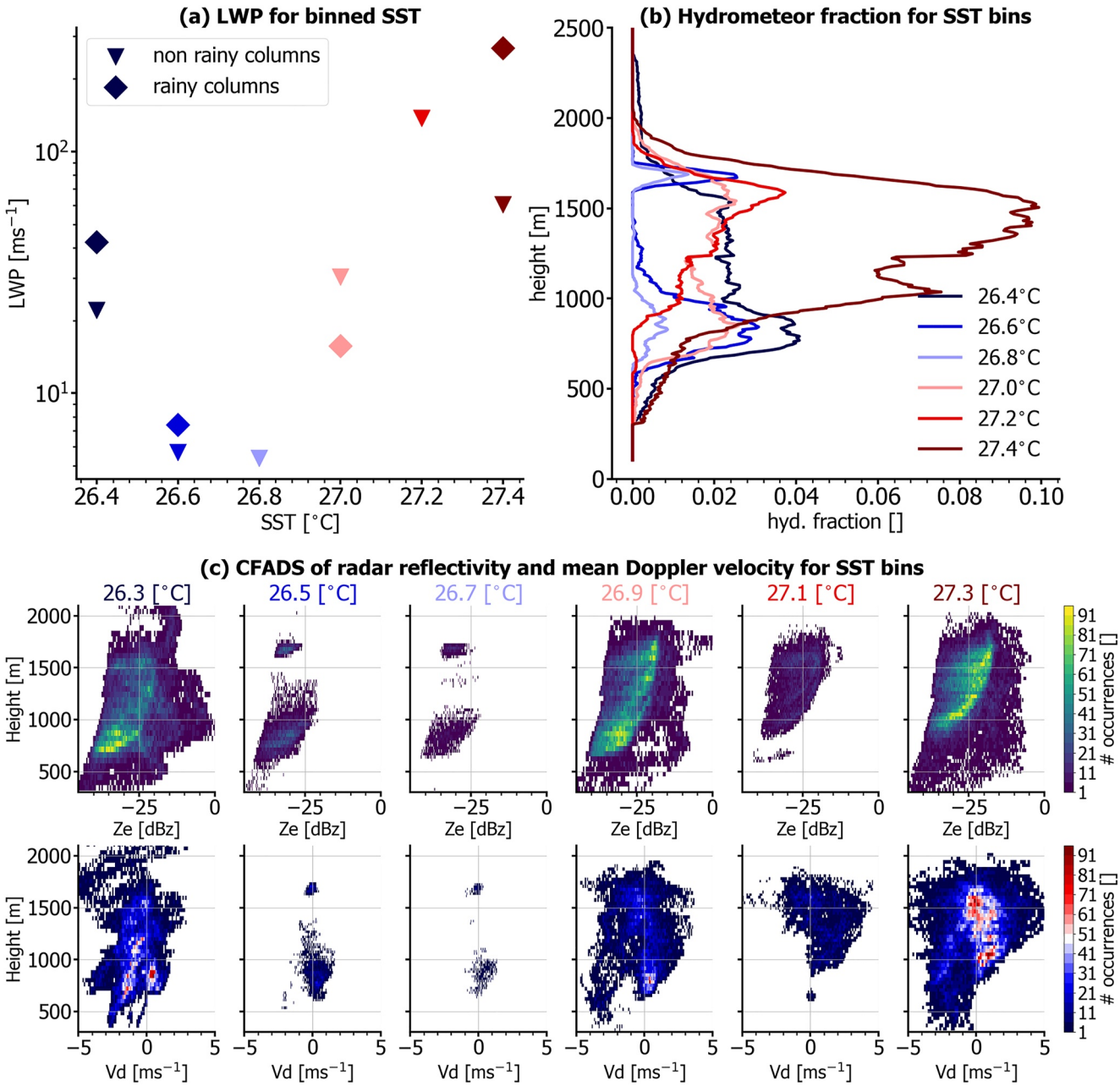


Figure 10. Radar-derived cloud properties binned over the thermosalinograph sea surface temperature: (a) liquid water path for non-rainy (triangles) and rainy columns (diamonds), (b) vertical profiles of hydrometeor fraction, and (c) contour frequency by altitude diagrams of radar reflectivity (first row) and mean Doppler velocity (second row).

toward warmer SST, (a) the separation between the two cloud peaks disappears and (b) the cloud base, the vertical extension of the cloud profiles and the cloudiness amount increase. The CFADs (Figure 10c) further confirm the previous analysis. For SST smaller than 26.7°C the Ze values (first row in Figure 10c) display an adiabatic profile that is not vertically extended, corresponding to shallow ABL clouds with cloud base below 700 m and smaller drops with Ze values almost all below −25 dBz. For SST larger than 26.7°C, instead, the Ze adiabatic profiles extend deeper in the boundary layer, reaching almost 2,000 m. The larger cloud vertical extension allows the formation of larger drops with Ze > −25 dBz via diffusion of water vapor on the drops' surface. Note that the adiabatic profile is a theoretical curve that can be derived assuming that: (a) the droplet number concentration is invariant and (b) LWP is distributed in the cloud profile scaling adiabatically (Knist, 2014). Cloud base appears to

21698996, 2022, 21, Downloaded from https://agupubs.onlinelibrary.wiley.com/doi/10.1029/2022JD036799 by Cochrane France, Wiley Online Library on [02/12/2022]. See the Terms and Conditions (https://onlinelibrary.wiley.com/terms-and-conditions) on Wiley Online Library for rules of use; OA articles are governed by the applicable Creative Commons License

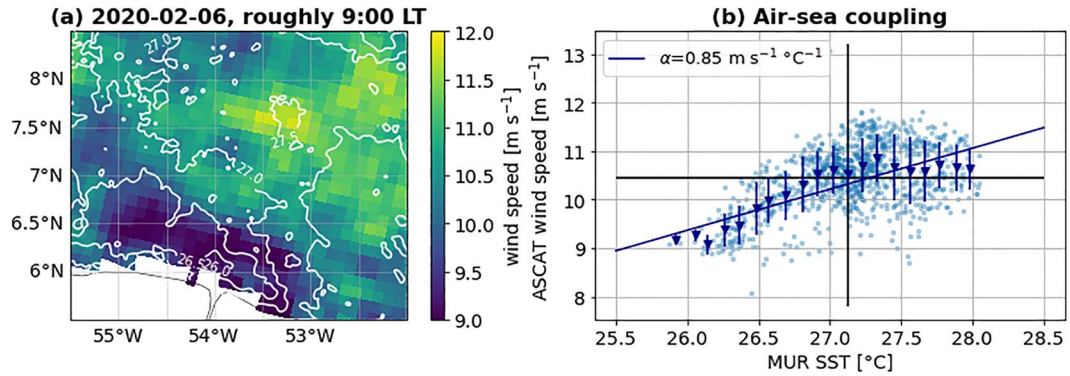


Figure 11. (a) Instantaneous wind speed from the Advanced SCATterometer instrument on Metop-B (colors) and Multi-scale Ultra-high Resolution sea surface temperature map (white contours) on the 6th of February 2020. (b) Scatter plot and binned scatter plot (mean and standard deviation for each bin shown with the triangles and the error bars, respectively) of the two variables shown in panel (a). The solid line shows the least square linear regression computed on the binned scatter plot, with the value of the slope printed in the legend.

be higher over warmer waters. The mean Doppler velocity observations (second row in Figure 10c) represent, in a first approximation, a convolution of the droplet speed and the air motion and on average. The Vd CFAD highlights stronger updrafts across the vertical cloud profile for warm SSTs, that make the clouds develop to a thicker layer. Also the vertical velocity observations from DL support this hypothesis. These stronger updraft motions, bringing water vapor above the LCL, promote condensation and are a net sink of water vapor. Once cloud droplets are formed and advected away, the local amount of water vapor decreases. Thus, not only the surface WVMR is reduced over warm SST because the vertical mixing enhances the ABL-top entrainment, but also because there is more condensation. This process possibly feeds back on the LHF, that is maintained high over warm SST and promotes further surface evaporation. However, possible competing effects exists. For example, the ABL-top mixing reduces the humidity gradient between the sub-cloud and cloud layers. Thus, the drying effect of the entrainment is less efficient.

Our results are in agreement with the observations of de Szoeke et al. (2021). They find that, in the tropical Indian ocean, the SST forcing is responsible for the enhanced vertical mixing in the maritime ABL when the wind is weak, and a strong SST diurnal warming occurs. The mixing exports WVMR above the LCL, promoting low-level cloud formation. In our case study, we observe a similar behavior. However, for us the variability in the SST that generates the cloud response is not due to the temporal evolution but to the spatial mesoscale structure visible in Figure 1. We observe a 1 K difference on the two sides of the front, that is comparable to their SST variability.

4. Satellite Analysis

As the ship-borne instruments only measure a single point in space per instant, we try to increase the robustness of the detected surface wind and cloud response by considering some relevant satellite observations. Ship-borne measurements revealed a surface wind response over the cold SST patch in agreement with the DMM mechanism: surface wind slows down over the cold SST because of the higher stability of the air column and the corresponding vertical decoupling of the wind structure. We consider Level-2 wind speed maps from the Advanced SCATterometer (ASCAT) instrument on the METeorological OPerational (Metop-B) satellite at the beginning of February 2020 to test whether a similar response is visible in satellite data. We analyze ASCAT data and corresponding MUR SST data (white dashed rectangle shown in Figure 1a) from the 6th of February 2020 because no data were available between the 2nd and 3rd of February 2020. These data are available from the NASA JPL PODAAC platform (https://podaac.jpl.nasa.gov/, last accessed: March 2022) and are given on an irregular grid with a 12.5 km nominal grid spacing.

An evident slow down of the surface wind appears in correspondence of the cold SST patch, which corroborates the fact that DMM can play a significant role in modulating the surface wind speed in this region at this time of the year (Figure 11a). This is confirmed by the positive coupling coefficient computed between the wind and

21698996, 2022, 21, Downloaded from https://agupubs.onlinelibrary.wiley.com/doi/10.1029/2022JD036799 by Cochrane France, Wiley Online Library on [02/12/2022]. See the Terms and Conditions (https://onlinelibrary.wiley.com/terms-and-conditions) on Wiley Online Library for rules of use; OA articles are governed by the applicable Creative Commons License

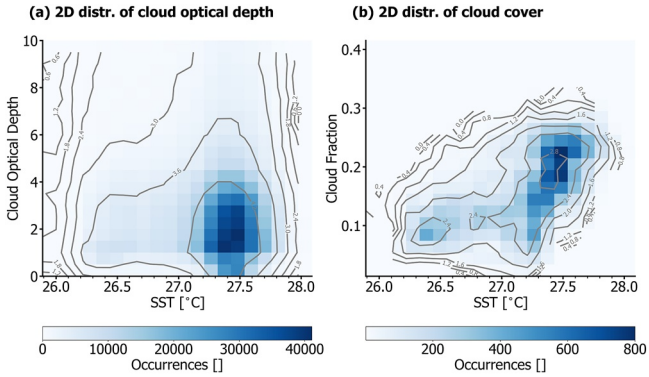


Figure 12. Bi-dimensional distributions of Multi-scale Ultra-high Resolution sea surface temperature VS cloud cover (a) and cloud optical depth (b) derived from GOES-East observations over the 2 days of interest. Colors show the actual number of occurrences and the contours show its logarithm, to highlight lower values. In panel (a) the occurrences of Cloud Optical Depth is directly shown, whereas in panel (b) the binary cloud mask (BCM) is used to compute the cloud fraction defined as the temporal average of the BCM over the 2 days of interest.

SST fields in the area of interest (Figure 11b). The coupling coefficient is the slope of the least square linear regression of the binned scatter plot of the two fields and is found to be relatively high here, as typical values from satellite data are 0.5 m s^{-1}/°C^{-1} (Song et al., 2009). Surely, a single map is not enough to claim that the response is statistically significant, but ongoing efforts suggest that this is the case. A detailed analysis on long-term statistics of this kind of atmospheric response goes beyond the scope of the present work and will be the object of a future study. Efforts are ongoing to characterize the atmospheric response to the SST as a function of different environmental conditions using high-resolution models, instantaneous co-located wind and SST satellite data, and estimates of turbulent heat fluxes.

To further extend the cloud response observed from the ship-borne instruments, we consider 2 days of data (2nd and 3rd of February 2020) from the Geostationary Operational Environmental Satellite - East (GOES-East) satellite. They are provided at 2 km grid spacing every 10 min. In particular, we use the Binary Cloud Mask (BCM) and the Cloud Optical Depth (COD) products from the GOES-R Advanced Baseline Imager (Schmit et al., 2017), available at https://www.ncei.noaa.gov/products/satellite/goes-r-series (last accessed: December 2021). We crop the data over the area shown as a white dashed rectangle in Figure 1a. Over the cold patch (for SST values roughly smaller than 26.75°C) we observe fewer (CF < 0.15, Figure 12a) thin clouds (COD < 4, Figure 12b). For warmer SSTs, the cloud fraction steadily increase up to 0.3, and clouds are also optically thicker. Movies S1, S2, and S3 provide more details on the described signal on the thicker and more frequent clouds observed over the warm water.

5. Conclusions

For the first time within the EUREC^{4}A framework, high-resolution ship-based remote sensing and in situ instruments (ARTHUS Raman lidar, DLs, W-band radar, RSs) were operated at open-sea to reveal unseen details in the ABL structure and clouds. Here, we exploited such a large variety of observations to provide insights into the interactions between the SST anomalies in the ocean and the ABL atmospheric and cloud response.

We adopted a synergistic approach that merged and integrated the extremely high-resolution information from different instruments to draw a comprehensive picture of the air-sea interaction processes. To better isolate the impact of the SST from the signal caused by the DC and the large-scale variability, we applied some post-processing to the data. When possible, we calculated the DC of the variables of interest and removed it from the signal, obtaining the daily anomaly in this way. To remove the large-scale variability, we characterized it using ERA5 data extracted over two separate areas located over the warm and cold SST patches. Finally, we excluded the observations collected during rainy conditions because rain can affect the ABL measurements and alter the interpretation of the signal generated by the SST structure.

Satellite data reveal a homogeneous north-easterly wind flow over the cold patch. We measure an intensified vertical wind velocity mixing over the warm SST region, primarily evident in the sub-cloud layer. Horizontal wind speed measured by RS and DL gets reduced over the cold patch, in agreement with the DMM mechanism. The 3–4 m s^{-1} difference in surface observed wind speed over warm and cold SST waters cannot be entirely ascribed to the large-scale dynamics that only accounts for a 1 m s^{-1} surface reduction. In the observations, we also detect a shallower and more humid ABL over the cold SST. In this case, ERA5 profiles and observations differ at the surface. We argue that ERA5 might not properly represent the ABL mixing, resulting in a disagreement of the amount of WVMR with respect to the RSs, which agree with bulk modeling results.

The LHF over warm SST is stronger than on cold SST. Two main reasons account for this result: (a) the wind accelerates because of the DMM mechanism, as described above and (b) the deepening of the ABL decreases the amount of water vapor at the surface by diluting it in the deeper ABL. A possible third mechanism could also play a role: in regions where ABLH overcomes the LCL, the process of cloud formation (and advection) is a net

21698996, 2022, 21, Downloaded from https://agupubs.onlinelibrary.wiley.com/doi/10.1029/2022JD036799 by Cochrane France, Wiley Online Library on [02/12/2022]. See the Terms and Conditions (https://onlinelibrary.wiley.com/terms-and-conditions) on Wiley Online Library for rules of use; OA articles are governed by the applicable Creative Commons License

exporter of water vapor, that is, a sink. This, however, is entangled with the modification of the vertical humidity gradient between the cloud and sub-cloud layers, which might affect the drying efficiency of the entrainment.

We observe shallower and more rare clouds over the cold patch. These low-level clouds grow deeper in the ABL, forming a single cloud layer with higher water content and CBH over the warm SST. Moreover, while on the cold SST patch, LCL and ABLH reach the same height, on the warm patch, the ABLH is at least 200 m higher than the LCL, differing thus from Neggers et al. (2006), where the ABLH coincides with the LCL. However, our results agree with de Szoeke et al. (2021).

To support and extend the results obtained from the ship-based remote sensing observations, some preliminary analyses on the response to SST cold patch detected from satellite sensors were also performed. Using a map from the closest day to the presented analyses, we find that the surface wind speed slows down on the cold SST patch. The cloud cover for the same period of the analyses increases with SST, as well as the COD. As a detailed analysis of long-term statistics of such atmospheric responses using satellite data goes beyond the scope of the present work, we plan to focus our research efforts in this direction for future studies.

Appendix A: Error Propagation for the Height-SST Sections of Rain-Free Daily Anomalies

Consider a section of a field $q = q(z, t)$, measured by Atmospheric Raman Temperature and Humidity Sounder or a Doppler lidar, given as a function of the height z and time t, with its constant and uniform uncertainty σ_q. The field q could be water-vapor mixing ratio (WVMR), air temperature, a wind component, latent heat flux or sensible heat flux, for example, When computing its diurnal cycle (DC), the uncertainty propagates as in computing an arithmetic mean and depends on the number of values considered in each bin of height z and time of the day τ, denoted with $N_{\mathrm{DC}}(z, \tau)$, as

$$\sigma_{qDC}(z, \tau) = \frac{\sigma_q}{\sqrt{N_{DC}(z, \tau)}}. \tag{A1}$$

With a conservative approach, N_{DC} can be taken to be the number of days used to estimate the DC N_{days}, so that

$$\overline{\sigma}_{qDC} = \frac{\sigma_q}{\sqrt{N_{days}}}. \tag{A2}$$

The uncertainty on the daily anomaly $q'(z, t) = q(z, t) - q_{DC}(z, \tau)$, then, is the square root of the sum of the original and the daily cycle squared uncertainties, namely

$$\sigma_{q'} = \sqrt{\sigma_q^2 + \overline{\sigma}_{qDC}^2} = \sigma_q \sqrt{1 + \frac{1}{N_{days}}}. \tag{A3}$$

As, to obtain the height-sea surface temperature (SST) section of q', another arithmetic mean is computed, we can write that the uncertainty associated to the height-SST section $q^* = q^*(z, \mathrm{SST})$ is

$$\sigma_{q^*}(z, SST) = \frac{\sigma_q}{\sqrt{N^*(z, SST)}} \sqrt{1 + \frac{1}{N_{days}}}, \tag{A4}$$

where $N^*(z, \mathrm{SST})$ is the number of values in each height-SST bin. In the final height-SST section, then, we consider as significant a value that is different from zero by at least three times the value of its corresponding uncertainty $\sigma_{q^*}(z, SST)$.

Appendix B: Meteomodem and Vaisala RS Humidity Bias

Stephan et al. (2021) notice a relative humidity (RH) bias between Meteomodem and Vaisala radiosonde (RS) data, with Meteomodem detecting a RH 5% higher than Vaisala, considering RS profiles within a 25 min interval throughout the entire campaign. As no bias in temperature is detected, we can convert the RH bias in a WVMR bias noting that

21698996, 2022, 21, Downloaded from https://agupubs.onlinelibrary.wiley.com/doi/10.1029/2022JD036799 by Cochrane France, Wiley Online Library on [02/12/2022]. See the Terms and Conditions (https://onlinelibrary.wiley.com/terms-and-conditions) on Wiley Online Library for rules of use; OA articles are governed by the applicable Creative Commons License

$$q = q_s \frac{\mathrm{RH}}{100}, \tag{B1}$$

with q denoting the WVMR and q_s the saturation WVMR. The latter can be expressed as a function of the dry air pressure p_d and temperature T with the Clausius-Clapeyron equation, namely

$$q_s = \epsilon \frac{e_{s0}}{p_d} \exp\left[\frac{L_v}{R_v}\left(\frac{1}{T_0} - \frac{1}{T}\right)\right], \tag{B2}$$

with $\epsilon = R_d/R_v = 0.622$ being the ratio between the dry air and the water vapor gas constants, $R_d = 287\ \mathrm{J\ K^{-1}\ kg^{-1}}$ and $R_v = 461\ \mathrm{J\ K^{-1}\ kg^{-1}}$, respectively, $L_v = 2.5 \times 10^6\ \mathrm{J\ kg^{-1}}$ being the latent heat of vaporization, and $e_{s0} = 6.11$ hPa and $T_0 = 273$ K two constants of integration. Thus, the relationship between the bias in RH, ΔRH, and the bias in WVMR, Δq, is

$$\Delta q = \epsilon \frac{e_{s0}}{p_d} \exp\left[\frac{L_v}{R_v}\left(\frac{1}{T_0} - \frac{1}{T}\right)\right] \frac{\Delta \mathrm{RH}}{100}, \tag{B3}$$

which is roughly 1 g kg^{-1} for typical values of p_d and T in the atmospheric boundary layer (1,000 hPa and 25°C, respectively).

Conflict of Interest

The authors declare no conflicts of interest relevant to this study.

Data Availability Statement

The multiple data sets used for deriving the results in this study are available at the Zenodo repository via https://doi.org/10.5281/zenodo.6365636 with license Creative Common Attribution 4.0 International (Acquistapace, Meroni, & Labbri, 2022). The codes used to produce the results presented in this work are publicly available at the open access platform Github at https://github.com/ClauClouds/SST-impact/.

Acknowledgments
This research has been supported by the Deutsche Forschungsgemeinschaft (Individual proposal, Project 437320342). We acknowledge the Deutsche Forschungsgemeinschaft for their support of the project "Precipitation life cycle in trade wind cumuli" (https://gepris.dfg.de/gepris/projekt/437320342, last access: 23 December 2021). A.N.M.'s research is supported by the European Space Agency (ESA) as part of the GLAUCO Climate Change Initiative fellowship (ESA ESRIN/Contract 4000133281/20/I/NB). The projects JPI Climate Oceans EUREC4A-OA and Progetto Dipartimenti di Eccellenza, funded by MIUR 2018–2022, are also acknowledged. This article is partially based upon work from COST Action PROBE, supported by COST (European Cooperation in Science and Technology), https://www.cost.eu/ (last access: 23 December 2021). The development of ARTHUS was supported by the Helmholtz Association of German Research Centers within the project Modular Observation Solutions for Earth Systems. We would also like to acknowledge the ship crews for the brilliant support offered in the installation of the equipment on board the R/V MS Merian and R/V L'Atalante and for facing all the technical issues encountered during the campaign. Dr. Johannes Karstensen, Prof. Sabrina Speich, and Dr. Rémi Laxenaire are particularly acknowledged for their efforts in the management of the scientific expeditions and the synergistic use of near-real-time satellite data that lead to the sampling of the cold patch considered in this work. Finally, we would like to thank Prof. Dr. Susanne Crewell, Prof. Sabrina Speich, Prof. Claudia Pasquero, and Dr. Fabien Desbiolles for the fruitful discussions. Open Access funding enabled and organized by Projekt DEAL.

References

Acquistapace, C., Coulter, R., Crewell, S., Garcia-Benadi, A., Gierens, R., Labbri, G., et al. (2022). EUREC^{4}A's *Maria S. Merian* ship-based cloud and micro rain radar observations of clouds and precipitation. *Earth System Science Data*, *14*(1), 33–55. https://doi.org/10.5194/essd-14-33-2022

Acquistapace, C., Meroni, A., & Labbri, G. (2022). Dataset for the "Fast atmospheric response to a cold oceanic mesoscale patch in the north-western tropical Atlantic" publication [Dataset]. Zenodo. Retrieved from https://zenodo.org/deposit/6365636

Behrendt, A., Wulfmeyer, V., Senff, C., Muppa, S. K., Späth, F., Lange, D., et al. (2020). Observation of sensible and latent heat flux profiles with lidar. *Atmospheric Measurement Techniques*, *13*(6), 3221–3233. https://doi.org/10.5194/amt-13-3221-2020

Bony, S., & Dufresne, J.-L. (2005). Marine boundary layer clouds at the heart of tropical cloud feedback uncertainties in climate models. *Geophysical Research Letters*, *32*(20), L20806. https://doi.org/10.1029/2005GL023851

Bony, S., Schulz, H., Vial, J., & Stevens, B. (2020). Sugar, gravel, fish, and flowers: Dependence of mesoscale patterns of trade-wind clouds on environmental conditions. *Geophysical Research Letters*, *47*(7), e2019GL085988. https://doi.org/10.1029/2019GL085988

Bony, S., Stevens, B., Ament, F., Bigorre, S., Chazette, P., Crewell, S., et al. (2017). EUREC^{4}A: A field campaign to elucidate the couplings between clouds, convection and circulation. *Surveys in Geophysics*, *38*(6), 1529–1568. https://doi.org/10.1007/s10712-017-9428-0

Bretherton, C. S., Blossey, P. N., & Jones, C. R. (2013). Mechanisms of marine low cloud sensitivity to idealized climate perturbations: A single-LES exploration extending the CGILS cases. *Journal of Advances in Modeling Earth Systems*, *5*(2), 316–337. https://doi.org/10.1002/jame.20019

Brueck, M., Nuijens, L., & Stevens, B. (2015). On the seasonal and synoptic time-scale variability of the North Atlantic trade wind region and its low-level clouds. *Journal of the Atmospheric Sciences*, *72*(4), 1428–1446. https://doi.org/10.1175/JAS-D-14-0054.1

Ceppi, P., Brient, F., Zelinka, M. D., & Hartmann, D. L. (2017). Cloud feedback mechanisms and their representation in global climate models. *WIREs Climate Change*, *8*(4), e465. https://doi.org/10.1002/wcc.465

Cesana, G., Del Genio, A. D., Ackerman, A. S., Kelley, M., Elsaesser, G., Fridlind, A. M., et al. (2019). Evaluating models' response of tropical low clouds to SST forcings using CALIPSO observations. *Atmospheric Chemistry and Physics*, *19*(5), 2813–2832. https://doi.org/10.5194/acp-19-2813-2019

Cesana, G., & Waliser, D. E. (2016). Characterizing and understanding systematic biases in the vertical structure of clouds in CMIP5/CFMIP2 models. *Geophysical Research Letters*, *43*(19), 10538–10546. https://doi.org/10.1002/2016GL070515

Chen, L., Jia, Y., & Liu, Q. (2017). Oceanic eddy-driven atmospheric secondary circulation in the winter Kuroshio Extension region. *Journal of Oceanography*, *73*(3), 295–307. https://doi.org/10.1007/s10872-016-0403-z

Chin, T. M., Vazquez-Cuervo, J., & Armstrong, E. M. (2017). A multi-scale high-resolution analysis of global sea surface temperature. *Remote Sensing of Environment*, *200*, 154–169. https://doi.org/10.1016/j.rse.2017.07.029

21698996, 2022, 21, Downloaded from https://agupubs.onlinelibrary.wiley.com/doi/10.1029/2022JD036799 by Cochrane France, Wiley Online Library on [02/12/2022]. See the Terms and Conditions (https://onlinelibrary.wiley.com/terms-and-conditions) on Wiley Online Library for rules of use; OA articles are governed by the applicable Creative Commons License

Davison, J. L., Rauber, R. M., Di Girolamo, L., & LeMone, M. A. (2013). A revised conceptual model of the tropical marine boundary layer. Part I: Statistical characterization of the variability inherent in the wintertime trade wind regime over the western tropical Atlantic. *Journal of the Atmospheric Sciences*, *70*(10), 3005–3024. https://doi.org/10.1175/JAS-D-12-0321.1

Desbiolles, F., Alberti, M., Hamouda, M. E., Meroni, A. N., & Pasquero, C. (2021). Links between sea surface temperature structures, clouds and rainfall: Study case of the Mediterranean Sea. *Geophysical Research Letters*, *48*(10), e2020GL091839. https://doi.org/10.1029/2020GL091839

de Szoeke, S. P., Marke, T., & Alan Brewer, W. (2021). Diurnal ocean surface warming drives convective turbulence and clouds in the atmosphere. *Geophysical Research Letters*, *48*(4), e2020GL091299. https://doi.org/10.1029/2020GL091299

Frenger, I., Gruber, N., Knutti, R., & Münnich, M. (2013). Imprint of Southern Ocean eddies on winds, clouds and rainfall. *Nature Geoscience*, *6*(8), 608–612. https://doi.org/10.1038/ngeo1863

Gaube, P., Chickadel, C. C., Branch, R., & Jessup, A. (2019). Satellite observations of SST-induced wind speed perturbation at the oceanic submesoscale. *Geophysical Research Letters*, *46*(5), 2690–2695. https://doi.org/10.1029/2018GL080807

Hayes, S. P., McPhaden, M. J., & Wallace, J. M. (1989). The influence of sea-surface temperature on surface wind in the eastern equatorial Pacific: Weekly to monthly variability. *Journal of Climate*, *2*(12), 1500–1506. https://doi.org/10.1175/1520-0442(1989)002<1500:TIOSST>2.0.CO;2

Hersbach, H., Bell, B., Berrisford, P., Hirahara, S., Horányi, A., Muñoz-Sabater, J., et al. (2020). The ERA5 global reanalysis. *Quarterly Journal of the Royal Meteorological Society*, *146*(730), 1999–2049. https://doi.org/10.1002/qj.3803

Ignatov, A. (2010). GOES-R Advanced Baseline Imager (ABI) algorithm theoretical basis document for sea surface temperature. Retrieved from https://www.star.nesdis.noaa.gov/goesr/documents/ATBDs/Baseline/ATBD_GOES-R_SST-v2.0_Aug2010.pdf

Knist, C. (2014). Retrieval of liquid water cloud properties from ground-based remote sensing observations. Retrieved from https://repository.tudelft.nl/islandora/object/uuid:2a844dc9-0e89-43c7-a150-a89db0c8327b?collection=research

Küchler, N., Kneifel, S., Löhnert, U., Kollias, P., Czekala, H., & Rose, T. (2017). A W-band radar–radiometer system for accurate and continuous monitoring of clouds and precipitation. *Journal of Atmospheric and Oceanic Technology*, *34*(11), 2375–2392. https://doi.org/10.1175/JTECH-D-17-0019.1

Lange, D., Behrendt, A., & Wulfmeyer, V. (2019). Compact operational tropospheric water vapor and temperature Raman lidar with turbulence resolution. *Geophysical Research Letters*, *46*(24), 14844–14853. https://doi.org/10.1029/2019GL085774

Lenschow, D. H., Wulfmeyer, V., & Senff, C. (2000). Measuring second-through fourth-order moments in noisy data. *Journal of Atmospheric and Oceanic Technology*, *17*(10), 1330–1347. https://doi.org/10.1175/1520-0426(2000)017<1330:MSTFOM>2.0.CO;2

Li, Y., & Carbone, R. E. (2012). Excitation of rainfall over the tropical western Pacific. *Journal of the Atmospheric Sciences*, *69*(10), 2983–2994. https://doi.org/10.1175/JAS-D-11-0245.1

Lindzen, R. S., & Nigam, S. (1987). On the role of sea surface temperature gradients in forcing low-level winds and convergence in the tropics. *Journal of the Atmospheric Sciences*, *44*(17), 2418–2436. https://doi.org/10.1175/1520-0469(1987)044<2418:OTROSS>2.0.CO;2

Liu, X., Chang, P., Kurian, J., Saravanan, R., & Lin, X. (2018). Satellite-observed precipitation response to ocean mesoscale eddies. *Journal of Climate*, *31*(17), 6879–6895. https://doi.org/10.1175/JCLI-D-17-0668.1

Ma, J., Xu, H., Dong, C., Lin, P., & Liu, Y. (2015). Atmospheric responses to oceanic eddies in the Kuroshio Extension region. *Journal of Geophysical Research: Atmospheres*, *120*(13), 6313–6330. https://doi.org/10.1002/2014JD022930

Ma, Z., Fei, J., Lin, Y., & Huang, X. (2020). Modulation of clouds and rainfall by tropical cyclone's cold wakes. *Geophysical Research Letters*, *47*(17), e2020GL088873. https://doi.org/10.1029/2020GL088873

Mauger, G. S., & Norris, J. R. (2010). Assessing the impact of meteorological history on subtropical cloud fraction. *Journal of Climate*, *23*(11), 2926–2940. https://doi.org/10.1175/2010JCLI3272.1

McCoy, D. T., Eastman, R., Hartmann, D. L., & Wood, R. (2017). The change in low cloud cover in a warmed climate inferred from AIRS, MODIS, and ERA-Interim. *Journal of Climate*, *30*(10), 3609–3620. https://doi.org/10.1175/JCLI-D-15-0734.1

Meroni, A. N., Giurato, M., Ragone, F., & Pasquero, C. (2020). Observational evidence of the preferential occurrence of wind convergence over sea surface temperature fronts in the Mediterranean. *Quarterly Journal of the Royal Meteorological Society*, *146*(728), 1443–1458. https://doi.org/10.1002/qj.3745

Mieslinger, T., Horváth, A., Buehler, S. A., & Sakradzija, M. (2019). The dependence of shallow cumulus macrophysical properties on large-scale meteorology as observed in ASTER imagery. *Journal of Geophysical Research: Atmospheres*, *124*(21), 11477–11505. https://doi.org/10.1029/2019JD030768

Neggers, R., Stevens, B., & Neelin, J. D. (2006). A simple equilibrium model for shallow-cumulus-topped mixed layers. *Theoretical and Computational Fluid Dynamics*, *20*(5–6), 305–322. https://doi.org/10.1007/s00162-006-0030-1

Pasquero, C., Desbiolles, F., & Meroni, A. N. (2021). Air-sea interactions in the cold wakes of tropical cyclones. *Geophysical Research Letters*, *48*(2), e2020GL091185. https://doi.org/10.1029/2020GL091185

Pearson, G., Davies, F., & Collier, C. (2009). An analysis of the performance of the UFAM pulsed Doppler lidar for observing the boundary layer. *Journal of Atmospheric and Oceanic Technology*, *26*(2), 240–250. https://doi.org/10.1175/2008JTECHA1128.1

Perlin, N., de Szoeke, S. P., Chelton, D. B., Samelson, R. M., Skyllingstad, E. D., & O'Neill, L. W. (2014). Modeling the atmospheric boundary layer wind response to mesoscale sea surface temperature perturbations. *Monthly Weather Review*, *142*(11), 4284–4307. https://doi.org/10.1175/MWR-D-13-00332.1

Reverdin, G., Olivier, L., Foltz, G. R., Speich, S., Karstensen, J., Horstmann, J., et al. (2021). Formation and evolution of a freshwater plume in the northwestern tropical Atlantic in February 2020. *Journal of Geophysical Research: Oceans*, *126*(4), e2020JC016981. https://doi.org/10.1029/2020JC016981

Romps, D. M. (2017). Exact expression for the lifting condensation level. *Journal of the Atmospheric Sciences*, *74*(12), 3891–3900. https://doi.org/10.1175/JAS-D-17-0102.1

Rouault, M., Verley, P., & Backeberg, B. (2016). Wind changes above warm Agulhas Current eddies. *Ocean Science*, *12*(2), 495–506. https://doi.org/10.5194/os-12-495-2016

Savazzi, A. C. M., Nuijens, L., Sandu, I., George, G., & Bechtold, P. (2022). The representation of winds in the lower troposphere in ECMWF forecasts and reanalyses during the EUREC4A field campaign. *Atmospheric Chemistry and Physics Discussions*, *22*(19), 1–29. https://doi.org/10.5194/acp-2021-1050

Schmit, T. J., Griffith, P., Gunshor, M. M., Daniels, J. M., Goodman, S. J., & Lebair, W. J. (2017). A closer look at the ABI on the GOES-R series. *Bulletin of the American Meteorological Society*, *98*(4), 681–698. https://doi.org/10.1175/BAMS-D-15-00230.1

Scott, R. C., Myers, T. A., Norris, J. R., Zelinka, M. D., Klein, S. A., Sun, M., & Doelling, D. R. (2020). Observed sensitivity of low-cloud radiative effects to meteorological perturbations over the global oceans. *Journal of Climate*, *33*(18), 7717–7734. https://doi.org/10.1175/JCLI-D-19-1028.1

Seidel, D. J., Zhang, Y., Beljaars, A., Golaz, J.-C., Jacobson, A. R., & Medeiros, B. (2012). Climatology of the planetary boundary layer over the continental United States and Europe. *Journal of Geophysical Research*, *117*(D17), D17106. https://doi.org/10.1029/2012JD018143

21698996, 2022, 21, Downloaded from https://agupubs.onlinelibrary.wiley.com/doi/10.1029/2022JD036799 by Cochrane France, Wiley Online Library on [02/12/2022]. See the Terms and Conditions (https://onlinelibrary.wiley.com/terms-and-conditions) on Wiley Online Library for rules of use; OA articles are governed by the applicable Creative Commons License

Shao, M., Ortiz-Suslow, D. G., Haus, B. K., Lund, B., Williams, N. J., Ozgokmen, T. M., et al. (2019). The variability of winds and fluxes observed near submesoscale fronts. *Journal of Geophysical Research: Oceans*, *124*(11), 7756–7780. https://doi.org/10.1029/2019JC015236

Skyllingstad, E. D., Vickers, D., Mahrt, L., & Samelson, R. (2007). Effects of mesoscale sea-surface temperature fronts on the marine atmospheric boundary layer. *Boundary-Layer Meteorology*, *123*(2), 219–237. https://doi.org/10.1007/s10546-006-9127-8

Small, R., de Szoeke, S., Xie, S., O'Neill, L., Seo, H., Song, Q., et al. (2008). Air–sea interaction over ocean fronts and eddies. *Dynamics of Atmospheres and Oceans*, *45*(3), 274–319. https://doi.org/10.1016/j.dynatmoce.2008.01.001

Song, Q., Chelton, D. B., Esbensen, S. K., Thum, N., & O'Neill, L. W. (2009). Coupling between sea surface temperature and low-level winds in mesoscale numerical models. *Journal of Climate*, *22*(1), 146–164. https://doi.org/10.1175/2008JCLI2488.1

Speich, S. (2020). EUREC4A_OA cruise. https://doi.org/10.17600/18000670

Stephan, C. C., Schnitt, S., Schulz, H., Bellenger, H., de Szoeke, S. P., Acquistapace, C., et al. (2021). Ship- and island-based atmospheric soundings from the 2020 EUREC^{4}A field campaign. *Earth System Science Data*, *13*(2), 491–514. https://doi.org/10.5194/essd-13-491-2021

Stevens, B., Bony, S., Farrell, D., Ament, F., Blyth, A., Fairall, C., et al. (2021). EUREC^{4}A. *Earth System Science Data*, *13*(8), 4067–4119. https://doi.org/10.5194/essd-13-4067-2021

Sullivan, P. P., McWilliams, J. C., Weil, J. C., Patton, E. G., & Fernando, H. J. S. (2020). Marine boundary layers above heterogeneous SST: Across-front winds. *Journal of the Atmospheric Sciences*, *77*(12), 4251–4275. https://doi.org/10.1175/JAS-D-20-0062.1

Tomita, H., Xie, S.-P., Tokinaga, H., & Kawai, Y. (2013). Cloud response to the meandering Kuroshio Extension front. *Journal of Climate*, *26*(23), 9393–9398. https://doi.org/10.1175/JCLI-D-13-00133.1

Vogelezang, D. H. P., & Holtslag, A. A. M. (1996). Evaluation and model impacts of alternative boundary-layer height formulations. *Boundary-Layer Meteorology*, *81*(3), 245–269. https://doi.org/10.1007/BF02430331

Wallace, J. M., Mitchell, T. P., & Deser, C. (1989). The influence of sea-surface temperature on surface wind in the eastern equatorial Pacific: Seasonal and interannual variability. *Journal of Climate*, *2*(12), 1492–1499. https://doi.org/10.1175/1520-0442(1989)002<1492:TIOSST>2.0.CO;2

Wang, Q., Zhang, S.-P., Xie, S.-P., Norris, J. R., Sun, J.-X., & Jiang, Y.-X. (2019). Observed variations of the atmospheric boundary layer and stratocumulus over a warm eddy in the Kuroshio Extension. *Monthly Weather Review*, *147*(5), 1581–1591. https://doi.org/10.1175/MWR-D-18-0381.1

Wang, Z., & Sassen, K. (2001). Cloud type and macrophysical property retrieval using multiple remote sensors. *Journal of Applied Meteorology*, *40*(10), 1665–1682. https://doi.org/10.1175/1520-0450(2001)040<1665:CTAMPR>2.0.CO;2

Wulfmeyer, V., Muppa, S. K., Behrendt, A., Hammann, E., Späth, F., Sorbjan, Z., et al. (2016). Determination of convective boundary layer entrainment fluxes, dissipation rates, and the molecular destruction of variances: Theoretical description and a strategy for its confirmation with a novel lidar system synergy. *Journal of the Atmospheric Sciences*, *73*(2), 667–692. https://doi.org/10.1175/JAS-D-14-0392.1

Yuan, T., Oreopoulos, L., Platnick, S. E., & Meyer, K. (2018). Observations of local positive low cloud feedback patterns and their role in internal variability and climate sensitivity. *Geophysical Research Letters*, *45*(9), 4438–4445. https://doi.org/10.1029/2018GL077904

Zelinka, M. D., Myers, T. A., McCoy, D. T., Po-Chedley, S., Caldwell, P. M., Ceppi, P., et al. (2020). Causes of higher climate sensitivity in CMIP6 models. *Geophysical Research Letters*, *47*(1), e2019GL085782. https://doi.org/10.1029/2019GL085782

Zhang, J., Lin, Y., & Ma, Z. (2021). Footprint of tropical cyclone cold wakes on top-of-atmosphere radiation. *Geophysical Research Letters*, *48*(19), e2021GL094705. https://doi.org/10.1029/2021GL094705

Zheng, Y. (2019). Theoretical understanding of the linear relationship between convective updrafts and cloud-base height for shallow cumulus clouds. Part I: Maritime conditions. *Journal of the Atmospheric Sciences*, *76*(8), 2539–2558. https://doi.org/10.1175/JAS-D-18-0323.1

21698996, 2022, 21, Downloaded from https://agupubs.onlinelibrary.wiley.com/doi/10.1029/2022JD036799 by Cochrane France, Wiley Online Library on [02/12/2022]. See the Terms and Conditions (https://onlinelibrary.wiley.com/terms-and-conditions) on Wiley Online Library for rules of use; OA articles are governed by the applicable Creative Commons License